THE WAKSMAN FOUNDATION OF JAPAN INC.

Honorary Patron

H.I.H. Prince Akishino

Board of Directors

Chairman : Ichiro Kitasato, Adviser, The Kitasato Institute.
Former Chairman of The Board, Meiji Seika Kaisha, Ltd.
Satoshi Omura, Honorable Emeritus Professor, Kitasato Univ.
Takeji Nishikawa, Prof. Emeritus, Keio Univ.
Shoji Kudoh, Chairman, Board of Directors Japan Anti-Tuberdulosis Association.
Kakutaro Kitashiro, Chair of the Board of Trustees, International Christian University

Managing Director : Yuko Kitagawa, Prof., Keio Univ. Sch. Med.

Comptroller : Shirow Enoki, Former President, Seikagaku Corporation.
Masahiro Koya, President, Keio University Press Inc.

Councilors

Keizo Takemi, Member,The House of Councilors.
Koichi Yamanishi,, Director General,The Research Foundation for Microbial Diseases of Osaka Unoversity.
Shigeo Koyasu, Executive Director, RIKEN.
Takashi Shoda, Senior Corporate Adviser, Daiichi Sankyo Co., Ltd.
Tadakatsu Shimamura, Prof. Emeritus, Showa Univ.
Yoshinobu Sumiyama, Chairman of the Board of Directors, Toho University.
Professor Emeritus, Toho University.
Satoshi Iwata, National Cancer Center Hospital Director Dpartment of Infectious Diseases
Tsuneyo Mimori, Prof. Department of Rheumatology and Clinical Immunology Graduate School of Medicine, Kyoto University

Special Adviser

Akira Uehara, Chairman & CEO, Taisho Pharmaceutical Holdings Co., Ltd.
Osamu Nagayama, Chairman & CEO, Chugai Pharmaceutical Co., Ltd.
Haruo Naito, President & CEO, Eisai Pharmaceutical Co., Ltd.
Seiichi Sato, President & CEO, Sato Pharmaceutical Co., Ltd.
Yoshihiro Miwa, President & CEO, Kowa Co., Ltd.

２０１８

Published by
THE WAKSMAN FOUNDATION OF JAPAN INC.
26-1 Daikyo-cho, Shinjuku-ku,
Tokyo 160-0015, Japan
https://www.waksman.or.jp/

Preface to the First Report (1962)

It is indeed a privilege to take this opportunity to write a few words of introduction to the first report of the Waksman Foundation of Japan Inc., covering five years of its activities and comprising the results of the work of the first two years of research carried out by various scholars in Japan in the fields of microbiology and medical science, supported by this Foundation.

In 1952, I accepted the invitation from Keio University and the Kitasato Institute, to deliver the centennial lecture in honor of the great Japanese bacteriologist, Shibasaburo Kitasato. Before departing for Japan, I proposed to the trustees of the Rutgers Research and Educational Foundation which owned the patents on streptomycin, to share the royalties under the patent in Japan, for the support of research in microbiology and allied fields in that country. The trustees heartily approved my recommendation that I make such announcement to that effect.

Soon upon my arrival in Japan (December 17, 1952), I invited a group of eminent microbiologists, biochemists, and clinical investigators to meet with me in order to discuss the plan. Everyone present was very enthusiastic about the proposal. It was decided that a proper committee be selected to work out the plan of a Foundation under which the royalties were to be received and distributed for the support of Japanese investigators working in different universities in Japan and elsewhere, in the fields of microbiology and medical research. The committee recommended that a Board of Directors be selected and the proposed Foundation be named THE WAKSMAN FOUNDATION OF JAPAN INCORPORATION.

The Rutgers Research and Educational Foundation approved at once the above recommendations and issued a statement, signed by Dr. Lewis Webster Jones, President of the Foundation, to the effect that

"The Rutgers Research and Educational Foundation desires to emphasize that its principal concern is the advancement of scientific knowledge in the public interest and that it confidently expects that the Waksman Foundation for Microbiology and Medical Research in Japan will be similarly motivated, thereby serving the peoples of both countries."

This announcement was received with enthusiasm both by the scientific world and the popular press in Japan and in the United States. It took several years before the Waksman Foundation of Japan Inc. was properly organized, and before applications were received and approved. In 1958, I had the privilege of participating in the first official

meetings of the Board of Directors of the Japanese Foundation and to greet personally the first group of scholars to whom grants had been made.

In summarizing these brief remarks in connection with the first cinqueannual report of the Waksman Foundation of Japan Inc., I would like to enphasize that this example of collaboration between universities and scientists of the United States and Japan may serve to encourage collaboration between scientific workers throughout the world towards a better understanding between men and women and towards a happier and healthier human race, so that all the nations on this earth can live in peace and that man may finally "break his swords and build out of them plowshares" for the betterment of mankind as a whole.

Selman A. Waksman
Professor Emeritus
Rutgers-State University N. J., U. S. A.

The "Waksman Foundation of Japan Inc." was established in 1957 with the spirit of humanity by Dr. S.A. Waksman, Professor of Microbiology, Rutgers University, U.S.A. The Foundation's operations are possible only because Dr. S.A. Waksman and the Rutgers Research and Educational Foundation donated patent royalties he received from the production in Japan of the discovery, Streptomycin.

Because of these royalties, each year many Japanese scholars and research workers in the fields of Microbiology and medical science are encouraged and find it possible to continue their work. Especially, in accordance with Dr. Waksman's suggestion, the funds are distributed to scholars in local and economically hampered schools and laboratories and to those developing research workers who are endeavoring to expand in their fields. This thought of Dr. Waksman's is most appreciated, as it matches our Oriental phylosophy, and results in the search for a jewel among ordinary stones, which is the highest work of the science-leader.

Some five years have now passed since the start of this Foundation, and many persons have received aid through this period.

The reports which are presented herein cover the first and second group of research workers who received financial assistance from the Foundation.

Toshio Katow, M. D.
Executive Director

Contents

——Report of Researches in 2016, 2017, 2018——

Pathological Analyses in Constitutive Nrf2 Activation in The Liver

Keiko Taguchi

Department of Medical Biochemistry, Graduate School of Medicine, Tohoku University

2-1 Seiryo-machi, Aoba, Sendai, Miyagi 980-8575

Introduction

Nrf2 is a transcription factor that regulates expression of cytoprotective genes [1]. In the normal cells, Nrf2 is degraded by the ubiquitin-proteasome system. Keap1, an adaptor of Cullin3-based E3 ubiquitin ligase, binds to Nrf2 and ubiquitinate it. When cells are burdened with oxidative stress including electrophiles and reactive oxygen species (ROS), sulfhydryl groups in Keap1 are modified (**Fig. 1A**). Modified Keap1 loosens the binding to Nrf2 and released Nrf2 accumulates in the nucleus to bind to antioxidant responsive element (ARE) with small Maf (sMaf) [1]. The Nrf2 downstream gene products are mainly involved in cytoprotection including detoxication, anti-oxidation and metabolism. One of the representative Nrf2 target genes is NAD(P)H:quinone oxidoreductase (*Nqo1*). In these days, Nrf2 inducers are practical as therapeutic drugs and dietary supplements. Tecfidera® (dimethyl fumarate) is a drug for multiple sclerosis, and bardoxolone methyl (RTA 402, CDDO-Me) is in clinical trial as a drug for chronic kidney diseases. Sulforaphane extracted from broccoli sprout has been reported to protect from liver cancers in China.

Keap1 knockout mice with systematic Nrf2 activation show severe hyperkeratosis in digestive tracts including tongue, esophagus and forestomach [2]. For this reason, *Keap1* knockout mice are neonatal lethal. This phenotype is reproducible in epidermis-specific *Keap1* knockout mice, *Keap1*$^{flox/flox}$::*Keratin-Cre* mice [3]. Hyper-activation of Nrf2 in epidermis promotes cellular proliferation. Similarly, Nrf2 plays a role in proliferation in cancer cells. Using ChIP-seq and real-time PCR, several genes have been newly identified as Nrf2 target genes [4]; glucose-6-phosphate dehydrogenase (*G6pd*), phosphogluconate dehydrogenase (*Pgd*), transketolase (*Tkt*) and transaldolase 1 (*Taldo1*) responsible for pentose phosphate pathway (PPP), malic

enzyme 1 (*Me1*) and isocitrate dehydrogenase 1 (*Idh1*) responsible for NADPH synthesis. These genes are upregulated through conserved ARE in a Nrf2-dependent manner.

In most of human cancers, it has been found that Nrf2 is aberrantly activated (**Fig. 1B**) [1]. The disrupted binding of Keap1 and Nrf2 causes constitutive Nrf2 activation in cancer cells. There are several causes to disrupt the binding of Keap1 and Nrf2 in cancers; somatic mutations of *Keap1* or *Nrf2* genes, accumulation of disruptor proteins, silencing of *Keap1* due to the methylated promoter, and Keap1 protein modification by oncometabolites. So far, there is no evidence that constitutive Nrf2 activation itself causes carcinogenesis. In this study, aged liver-specific *Keap1* knockout (*Keap1*$^{flox/flox}$::*Albumin-Cre*; Keap1-Alb) mice were analyzed to examine whether constitutive Nrf2 activation is carcinogenic in the liver. Furthermore, whether administration of Nrf2 inducer, CDDO-Im, causes pathological changes was examined.

Materials and Methods

Animals

Keap1$^{flox/flox}$::*Albumin-Cre* (Keap1-Alb) mice [3, 5], *Pten*$^{flox/flox}$ (Control) mice as the control [6], wildtype rat and *Nrf2* knockout (Nrf2 KO) rat with a mutation of 1-bp insertion or 7-bp deletion [7] were provided water and labo MR Stock diet *ad libitum*. Rats were gavaged with 2-cyano-3,12-dioxooleana-1,9-dien-28-imidazolide (CDDO-Im; 30 μmol/kg body weight) and were sacrificed 6 hours after the single dose. For the multiple-dose, rats were gavaged with CDDO-Im (30 μmol/kg body weight) for 3 successive weeks on Monday, Wednesday, and Friday and were sacrificed 5 weeks after the last doses of CDDO-Im. All animals were maintained under semi-specific-pathogen-free conditions and treated according to the regulations of The Standards for Human Care and Use of Laboratory Animals of Tohoku University and Guidelines for Proper Conduct of Animal Experiments of the Ministry of Education, Culture, Sports, Science, and Technology of Japan. Blood and livers were harvested under anesthesia. Blood were centrifuged at 1,000 *g* for 5 min at 4°C. The obtained plasma was analyzed by FUJI DRI-CHEM7000 (FUJIFILM, Japan) to measure alanine transferase (ALT) and albumin (ALB).

Histological analyses

Livers were fixed in Mildform 10N (Wako Pure Chemical Industries, Ltd.) and embedded in paraffin. Masson Trichrome staining were performed according to a conventional method.

RNA purification and real-time PCR

Total RNA was isolated from the liver using ISOGEN (Nippon Gene) and transcribed into cDNA using SuperScript III Reverse Transcriptase (Life Technologies Corp., Carlsbad, CA). Quantitative PCR analysis was performed using the Applied Biosystems 7300 PCR system, and qPCR MasterMix Plus (Eurogentec). The data were normalized to ribosomal RNA (rRNA) expression.

Immunoblot analysis

The livers were homogenized in 9 volumes of 0.25 M sucrose, and the 10% homogenate was filtered through a 100 μm membrane. The nuclear fraction was prepared using Dignam's methods with some modifications. The cells were lysed in SDS sample buffer (50 mM Tris-HCl [pH 6.8], 10% glycerol and 2% SDS). The protein concentration was determined using a bicinchoninic acid (BCA) protein assay kit (Pierce Biotechnology, Rockford, IL), with bovine serum albumin as the standard. The samples were resolved using SDS-polyacrylamide gel electrophoresis and transferred onto a polyvinylidene difluoride membrane (Millipore, Billerica, MA). The following antibodies were used: anti-Nrf2, anti-Keap1, anti-Lamin B (Santa Cruz Biotechnology Inc., Dallas, TX, USA; sc-6217), anti-Nqo1 (Abcam plc., Cambridge, UK; ab2346) and anti-αTubulin (Sigma-Aldrich; T9026).

Statistical analysis

The average values were calculated, and the error bars indicate standard deviations. Differences were analysed using the Student's t test. $P < 0.05$ was considered statistically significant.

Results

Nrf2 is constitutively activated in the liver of Keap1-Alb mice

The liver of Keap1-Alb mice, Nrf2 is constitutively accumulated in the nucleus [3]. At first, whether Nrf2 activation was sustained in aged Keap1-Alb mice was confirmed. *Nqo1*, a representative Nrf2 target gene, was upregulated at 22-fold in Keap1-Alb mice at the age of 12 months (**Fig. 2A**). Constitutive Nrf2 activation was confirmed by the nuclear accumulation, accompanied by increased Nqo1 (**Fig. 2B**). Keap1 protein was completely diminished in Keap1-Alb mice livers. Therefore, Keap1-Alb mice are a proper model to examine an effect of constitutive Nrf2 activation *in vivo*.

Keap1-Alb mice show hepatomegaly and mild liver damage

Mice were sacrificed at the age of 6, 12 months and more. The liver size of Keap1-Alb mice gradually enlarged compared with those of Control mice (**Fig. 3A**). ALT, a marker of liver injury in plasma, tended to increase in Keap1-Alb mice at the age of more than 12 months (**Fig. 3B**). However, the extent was not severe at less than 100 U/L. ALB, a marker of liver function, was comparable in Control and Keap1-Alb mice (**Fig. 3C**). These data suggest that sustained Nrf2 activation gives rise to hepatomegaly and mild liver injury in the liver of Keap1-Alb mice.

Hepatic cysts appear in the peripheral area of Keap1-Alb livers from at the age of more than 12 months

Macroscopic observation indicated that hepatic cysts appeared in the peripheral area of Keap1-Alb livers from the age of 12 months and more (**Fig. 4A**). The size and number of cysts increased according to age. The phenotype was obvious at the age of 18 months. Control mice showed no macroscopic phenotype till the age of 24 months (**Fig. 4A**). Masson trichrome staining to discriminate collagen fibers showed that cholangiocytes around portal veins were increased in Keap1-Alb mice at the age of 12 months (**Fig. 4B**). In Keap1-Alb mice at the age of 18 months, hepatic cysts obviously appeared along with cholangiocyte expansion. Hyperplasia was observed in Keap1-Alb mice at the age of 24 months.

Single- or multiple-dose of CDDO-Im, a Nrf2 inducer, to wildtype and Nrf2 KO rats

CDDO-Im is a powerful Nrf2 inducer at a low concentration. Since hepatomegaly was observed in Keap1-Alb mice (**Fig. 3A**), pharmacological Nrf2 activation has a possibility to increase liver mass. Here, whether administration of CDDO-Im enlarges liver size or not was examined. Single dose of CDDO-Im had no effect on rate of liver to body weight (**Fig. 5A**). In multiple-dose of CDDO-Im, the liver size was comparable to that of vehicle-gavaged wildtype rats (**Fig. 5B**). The time point to analyze livers was 5 weeks after the multiple-dose. Just after the last dosing, the liver size should be measured to evaluate the effect of CDDO-Im on liver size. In contrast, livers of Nrf2 KO rats were significantly smaller than those of wildtype rats. Taken together, it is thought that Nrf2 is involved in maintenance of liver size. However, liver sizes of CDDO-Im-dosed wildtype rats did not increase in two patterns of dosing.

Discussion

Nrf2 is a well-known transcription factor that regulates cytoprotection. It has been reported that Nrf2 is constitutively activated in many types of cancer cells. *Nrf2* is one of genes with somatic mutations in liver cancers [8]. Nrf2 activation leads to proliferation in cancer cells. Nrf2 inhibitors have been developed as an anti-cancer drug in Nrf2-addicted cancer cells. These days, Nrf2 inducers are commercially used as therapeutic drugs and dietary supplements. The dose-response curve of Nrf2 activation is U-shaped, not linear. Too low or high activation of Nrf2 is a risk for cancers. *Keap1* knockout mice mimic high Nrf2 activation, but are neonatal lethal due to hyperkeratosis in esophagus and digestive tract. *Keap1* knockdown mice are a systematic Nrf2-activated model [3]. The liver is a main tissue to play important roles in detoxication and metabolism. Therefore, liver-specific Keap1-Alb mice were analyzed to examine liver-specific Nrf2 activation in this study. To evaluate safety in a use of Nrf2 inducers for a long time, we need examining the phenotype that constitutive Nrf2 activation gives rise to.

Liver-specific *Pten* and *Keap1* double knockout

(*Pten*$^{flox/flox}$::*Keap1*$^{flox/flox}$::*Albumin-Cre*, Pten:Keap1-Alb) mice aberrantly expand cholangiocytes around portal veins in an Nrf2-dependent manner [6]. This model mouse demonstrates that Nrf2 protein level is regulated by the ubiquitination and proteasomal degradation by Keap1-Cul3 complex and βTrCP-Cul1 complex. Pten deletion phosphorylates Akt and inactivates GSK3. In this situation, Nrf2 phosphorylation by GSK3 is stopped, and Nrf2 is released from the proteasomal degradation. Cholangiocytes are expanded in the liver of aged Keap1-Alb mice. One possibility of cholangiocyte expansion in Keap1-Alb mice is additional activation of Nrf2 by inactivated GSK3. Further analyses are needed to examine whether Pten-PI3K-Akt-GSK3 pathway is simultaneously activated in Keap1-Alb mice.

Liver cysts arise from aberrantly proliferative cholangiocytes accompanied by pericystic fibrosis and inflammation. Recently, it has been reported that Yes associated protein (YAP) activation is associated with hepatic cyst epithelial cell proliferation in autosomal recessive polycystic kidney disease (ARPKD), a rare but fatal genetic disease with progressive cyst development in the kidney and liver. When YAP is activated, YAP binds to different transcription factors to regulates expression of genes responsible for cell proliferation, cell survival, and apoptosis. One possibility of cyst formation is YAP activation in Keap1-Alb mice. However, there is no data of YAP activation in Keap1-Alb mice so far. In this study, the relationship between the Hippo pathway and Keap1-Nrf2 system has not been examined.

Genetic and constitutive Nrf2 activation by Keap1 deletion upregulates genes responsible for cytoprotection, leading to hepatomegaly, mild liver damage and hepatic cysts in liver-specific Keap1-Alb mice (**Fig. 6A**). Pharmacological and prolonged Nrf2 activation might be possible to lead to these phenotypes. However, single- or multiple-dose(s) of CDDO-Im did not increase liver mass. These suggest that the temporal dosing-induced Nrf2 activation might be safe in the liver. In order to evaluate safety of prolonged dosing of Nrf2 inducers as therapeutic drugs or dietary supplements, further experiments are expected. Dose control of Nrf2 inducers makes it possible to exert the pharmacological benefits without side effects (**Fig. 6B**).

Conclusion

Genetic and constitutive Nrf2 activation leads to hepatomegaly and mild liver damage in the liver. On the contrary, pharmacological and temporal Nrf2 activation did not change liver size in these conditions. Controlled dosing of Nrf2 inducers might exert pharmacological effects.

Acknowledgement

This research was kindly supported by Waksman Foundation of Japan INC.. These experiments were performed at Department of Medical Biochemistry, Graduate School Medicine, Tohoku University. The author would like to thank Professor Masayuki Yamamoto, co-workers and the Biomedical Research Core of Tohoku University Graduate School of Medicine for technical support.

Table 1. Primers and Probes used in the quantitative real-time PCR

Mouse Gene	Oligonucleotide
Nqo1-F	5'- AGCTGGAAGCTGCAGACCTG -3'
Nqo1-R	5'- CCTTTCAGAATGGCTGGCA -3'
Nqo1-P	5'- ATTTCAGTTCCCATTGCAGTGGTTTGGG -3'
rRNA-F	5'-CGGCTACCACATCCAAGGAA-3'
rRNA-R	5'-GCTGGAATTACCGCGGCT-3'
rRNA-P	5'-FAM-TGCTGGCACCAGACTTGCCCTC-TAMRA-3'

Figure 1

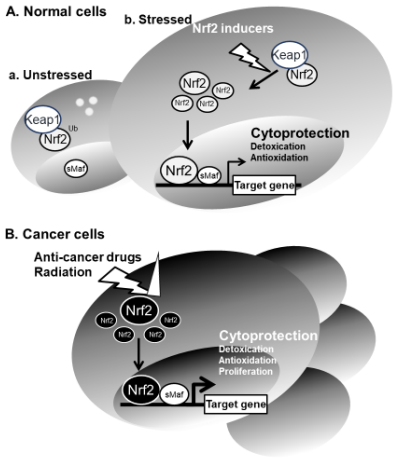

Figure 2

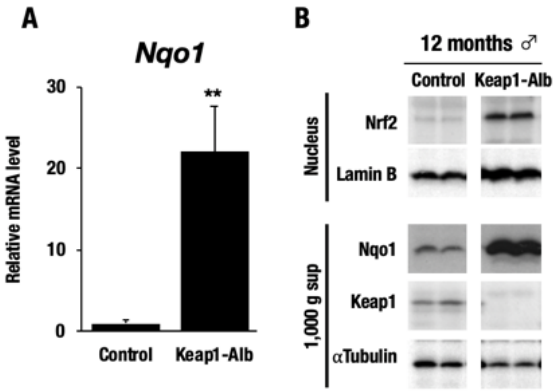

Fig. 1. Nrf2 activation in normal and cancer cells.

A. Unstressed- (a) and stressed- (b) normal cells. Nrf2 binds to Keap1 and is ubiquitinated immediately. Nrf2 inducers including electrophiles and reactive oxygen species (ROS) binds to sulfhydryl groups in Keap1. Nrf2 is accumulated in the nucleus and upregulates the downstream genes responsible for cytoprotection. **B.** Cancer cells. Nrf2-activated cancer cells are resistant against anti-cancer drugs and radiation. In addition, Nrf2 upregulates genes responsible for proliferation and metabolism.

Fig. 2. Constitutive Nrf2 activation in Keap1-Alb mice at the age of 12 months.

A. mRNA expression level of *Nqo1*. The data represent mean ± SD. **, $P < 0.01$. **B.** protein expression levels of Nrf2, Nqo1 and Keap1.

Figure 3

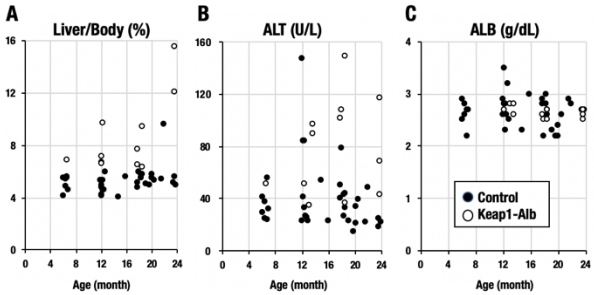

Figure 4

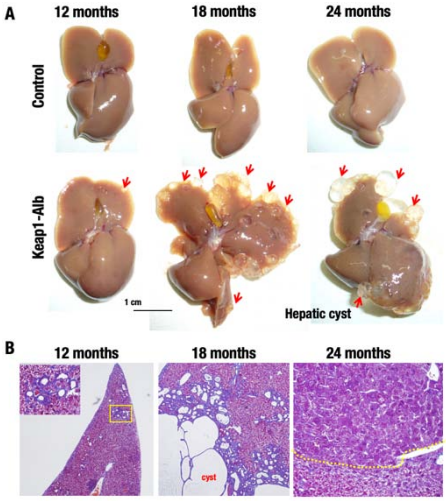

Fig. 3. Rates of liver weight to body weight and blood biochemical examination at the age of more than 12 months.

A. Rates of liver weight to body weight, **B.** Plasma ALT, **C.** Plasma ALB.

Fig. 4. Nrf2 activation causes hepatic cysts in the liver of Keap1-Alb mice at the age of more than 12 months.

A. Macroscopic morphology in Control and Keap1-Alb mice at the age of 12, 18 and 24 months. Arrows indicate hepatic cyst. **B.** Microscopic morphology in Control and Keap1-Alb mice at the age of 12, 18 and 24 months.

Figure 5

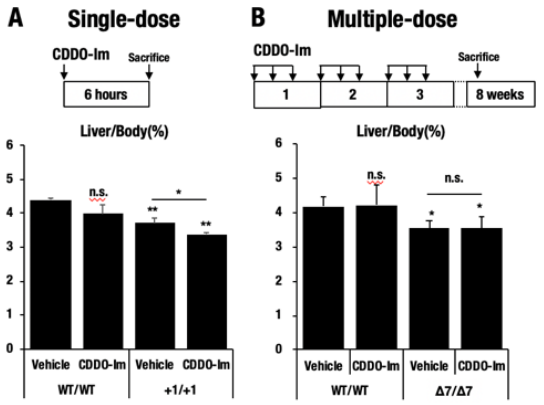

Figure 6

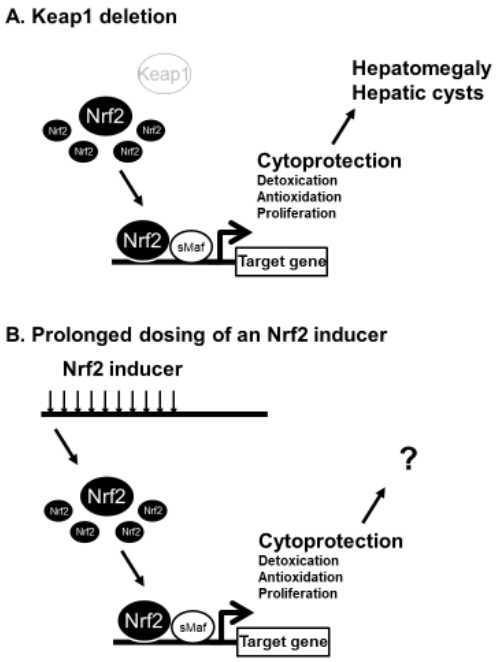

Fig. 5. Rates of liver weight to body weight in wildtype and Nrf2 KO rats administrated Nrf2 inducer, CDDO-Im.

A. Single-dose of CDDO-Im (30 μmol/kg body weight) for 6 hours to wildtype and Nrf2 KO (+1/+1) rats. **B.** Multiple-dose of CDDO-Im (30 μmol/kg body weight) for 3 successive weeks to wildtype and Nrf2 KO (Δ7/Δ7) rats. Rats were sacrificed 5 weeks after the last doses of CDDO-Im. The data represent mean ± SD. *, $P < 0.05$; **, $P < 0.01$; n.s., non-significant. Asterisks with brackets indicate the comparison between indicated groups.

Fig. 6. Constitutive Nrf2 activation in the liver of Keap1-Alb mice and prolonged dose of Nrf2 inducers.

A. Constitutive Keap1-Alb mice. **B.** Prolonged doses of Nrf2 inducers.

References

1) Taguchi, K. and Yamamoto, M. (2017) The KEAP1-NRF2 System in Cancer. Front Oncol, 7, 85.

2) Wakabayashi, N., Itoh, K., Wakabayashi, J., et al. (2003) Keap1-null mutation leads to postnatal lethality due to constitutive Nrf2 activation. Nat Genet, 35, 238-245.

3) Taguchi, K., Maher, J. M., Suzuki, T., Kawatani, Y., Motohashi, H., and Yamamoto, M. (2010). Genetic analysis of cytoprotective functions supported by graded expression of Keap1. Mol Cell Biol 30, 3016-3026.

4) Mitsuishi, Y., Taguchi, K., Kawatani, Y., et al. (2012) Nrf2 redirects glucose and glutamine into anabolic pathways in metabolic reprogramming. Cancer Cell, 22, 66-79.

5) Okawa, H., Motohashi, H., Kobayashi, A., et al. (2006) Hepatocyte-specific deletion of the keap1 gene activates Nrf2 and confers potent resistance against acute drug toxicity. *Biochem Biophys Res Commun*, **339**, 79-88.

6) Taguchi, K., Hirano, I., Itoh, T., et al. (2014) Nrf2 enhances cholangiocyte expansion in Pten-deficient livers. Mol Cell Biol, 34, 900-913.

7) Taguchi, K., Takaku, M., Egner, P.A., et al. (2016) Generation of A New Model Rat: Nrf2 Knockout Rats Are Sensitive to Aflatoxin B1 Toxicity. Toxicol Sci, 152, 40-52.

8) Taguchi, K., Motohashi, H., and Yamamoto, M. (2011) Molecular mechanisms of the Keap1-Nrf2 pathway in stress response and cancer evolution. Genes Cells, 16, 123-140

Visualization and functional assessment of IL-23 producing dendritic cells *in vivo*

Shinichiro Sawa

Division of Developmental Immunology, Institute for Genetic Medicine, Hokkaido University Sapporo, Hokkaido, Japan, 060-0815

Introduction

In 2000, Interleukin (IL-) 23 was discovered by researchers in DNAX Research Institute, as a heterodimeric cytokine composed by two units, p19 and IL12p40. Similar to IL-12, which is constituted of IL12p40 and p35, IL-23 is expressed predominantly by activated mononuclear phagocytic cells such as dendritic cells and phagocytes. Although p19 has sequence identity of approximately 40% to the p35 subunit of IL-12, p19 binds to the unique receptor, named IL-23R. The IL-23R is predominantly expressed on activated T cells both in mouse and human. IL-23R signal transduction studies revealed a constitutive association with Janus Kinase 2 (Jak2) and the predominant activation of Stat3.

From studies in a variety of mouse models, implication of $CD4^+$Th17 cell in autoimmune diseases was revealed. IL-23 pathway is essential for amplifying and stabilizing the pathogenic function of Th17 cells. Advances in genome-wide association studies (GWAS) across autoimmune and immune-mediated disorders have augmented our understanding of pathogenic mechanisms underlying these diseases. Among the IL-23 pathway genes, there reported multiple associations with SNPs within IL23R with multiple immune diseases, such as Inflammatory Bowel Disease (IBD), psoriasis, ankylosing spondylitis and psoriatic arthritis. The most notable genetic association of IL23R with most of these autoimmune diseases is the coding polymorphism Arg391Gln: the minor glutamine allele confers a two- to threefold increase in protection, compared to the more-common arginine allele, against developing IBD. This protective glutamine allele is a loss-of-function mutation resulting in decreased numbers of IL-23-dependent $CD4^+$Th17 cell in human cells.

Monoclonal antibodies against IL-12p40,

the cytokine subunit common to IL-12 and IL-23 are approved for the treatment of psoriasis, psoriatic arthritis and IBD. Monoclonal antibodies blocking the IL-23-specific p19 subunit have demonstrated promising results in Crohn's disease and psoriasis.

Recently, a new subset of lymphocyte termed group 3 innate lymphoid cell (ILC3) was discovered. Although ILC3 has no antigen specific T cell receptor, the spectrum of produced cytokine is close to that of Th17 cell. The development and the effector function of ILC3 is dependent on transcription factor RORγt. ILC3 expresses high level of IL-22 and contributes to the maintenance of intestinal barrier function in response to IL-23 via IL-23R expressed on the surface. It is known that ILC3s localize in the lamina propria of the intestine. However, in contrast to IL-23R-expressing lymphocytes, our knowledge about IL-23-expressing cell *in vivo* is quite limited.

Identification of actual IL-23 producing cell *in vivo* is critical for understanding development of $CD4^{+}$Th17-mediated autoimmune diseases and for clarifying precise cellular mechanism of ILC3-mediated intestinal barrier. Therefore, in this study, I aimed to visualize IL-23-expressing cell in IL-23p19 reporter mice.

Materials & Methods

Mice

Bacterial Artificial Chromosome (BAC)-transgenic *IL23a-Cre-ires-egfp*^{TG} mice were generated as described previously (Sparwasser, Genesis, 2004). The coding sequences for Cre and EGFP including the stop codons were tandemely ligated *via* encephalomyocarditis virus internal ribosome entry site (IRES) following SV40 polyA sequence and inserted into the exon 1 of *Il23a* in place of the endogenous ATG translation start codon, on a RP23-RP23-214N5 BAC (Invitrogen) carrying at least 50 kb of sequence upstream of the *Il23a* translation start site. The transgenic mice were backcrossed 5 times to C57BL/6J mice. Gt(ROSA)26Sor$^{tm14(CAG-tdTomato)/+}$ (Madisen, Nat Neurosci, 2010) were purchased from the Jackson laboratories and maintained on a C57BL/6J background. Mice were kept under specific pathogen-free conditions, and all the experiments were performed with the approval of the Institutional Review Board at the Hokkaido University.

Antibodies

The antibodies and chemicals used for flow cytometric analysis and immunohistochemistry were as follows. Pacific Blue anti-mouse CD45.2 (Clone104, Biolegend), Alexa Fluor 488 anti-mouse CX_3CR_1 (Clone SA011F11, Biolegend), PE-Cy7 anti-mouse CD11c (Clone N418 Biolegend), Biotin anti-mouse I-A/I-E antibody (Clone M5/114.15.2, Biolegend), Alexa 647 anti-mouse CD11b (Clone M1/70, Biolegend), anti-mouse CD103 (Clone 2E7, Biolegend) and Qdot™ 625 streptavidin conjugate (Q22063, ThermoFisher Scientific)

Histological Analysis

Cryosections of 10 μm were fixed with 4% Paraformaldehyde-containing PBS (pH7.4) overnight and stained immunohistochemically as described (Sawa et al. Nat Immunology, 2011). Whole mount images were taken by a fluorescence stereomicroscope (M165FC, Leica Inc.) and analyzed by the software LASX (Leica Inc.). Ileum were fixed, stained and observed using a confocal laser microscopy (LSM780, Carl Zeiss) and analyzed by the software Zen (Carl Zeiss Inc.). Nuclei were stained with 4'6-diamidiono-2-phenylindole (DAPI, Dojin-kagaku).

Isolation of cells from mouse tissues

For isolation of intestinal MNPs, 1cm-size small intestine longitudinally incised were first incubated in 30mM EDTA-containing PBS at room temperature for 10 min and wash with fresh EDTA-free PBS 10 times. After removal of Peyer's patches under stereomicroscope, tissues were munched with scissors and incubated for 30 min at 37 °C in DMEM (Gibco) containing 1.0 mg/ml Collagenase D (Roche), and 0.1 mg/ml DNase I (Invitrogen). Every 30min, tissues were washed with warm DMEM and re-incubated with fresh medium containing Collagenase D and DNase I. Supernatants were collected at each step. Debris was removed by the use of Percoll (GE Healthcare).

Flow cytometry

Nonspecific binding was blocked with 10% fetal bovine serum for 30 min. Dead cells

were distinguished with fixable viability dyes (eBioscience). Flow cytometric analysis and sorting was performed with BD Fortessa (BD Biosciences), BD FACSAriaIII (BD Biosciences) and Spectrum analyzer SA3800 (Sony). Data were analyzed using FlowJo software (Tree Star, Inc.).

Results

Visualization of IL23p19-expressed cell in the small intestine

In order to visualize IL-23a-expressing cells *in vivo*, we first observed EGFP expression of the whole intestine of *IL23a-Cre-ires-egfp*^{TG} mice. However, probably due to weak promoter activity of IL23a, it was impossible to directly identify EGFP-expressing cells in microscope (data not shown). We next tried to visualize cells that have history of IL-23a expression in IL23a-CIG BAC^{Tg}; R26-tdTomato-LSL mice. In this mice, Cre-mediated recombination induces constitutive expression of red-fluorescent protein, tdTomato, in cells that have the history of IL-23a expression (Figure 1-a). Stereomicroscopic analysis of the intestinal villi obtained from IL23a-CIG BAC^{Tg}; R26-tdTomato-LSL mice shows accumulation of tdTomato$^+$ cells (IL23-fm tdTomato$^+$ cell) in the intra-subepithelial region of villi in the whole intestine (Figure 1-b). Laser confocal microscopic analysis enabled us to identify morphology of these villus IL23-fm tdTomato$^+$ cells. In the intestinal villi, IL23-fm tdTomato$^+$ cells elongate their projections between epithelial cells as close as to the luminal surface (Figure 1-c).

Characterization of IL23p19-expressed cell

IL23-fm tdTomato$^+$ cells observed in the intestinal villi have similar morphology to previously reported $CX_3CR_1^+$ mononuclear phagocytes (MNPs) (Longman JEM, 2014). In order to characterize IL23-fm tdTomato$^+$ cell, we performed flow cytometry analysis obtained from small intestinal lamina propria (Figure 2). In the mononuclear cell fraction, both CD45$^+$ and CD45$^-$ cells were observed in IL23-fm tdTomato$^+$ cell fraction, suggesting that IL-23a is expressed both in hematopoietic and non-hematopoietic

compartments. Among IL23-fm tdTomato$^+$ cell fraction, 92% of CD45$^+$ cells were MHC class II ^{high} CD11c$^+$ dendritic cells. However, merely 10% of CD45$^+$ cells expressed CX_3CR_1 on their surface. These results suggest that IL-23p19 is expressed predominantly on $CX_3CR_1^-$ MHC classII ^{high} dendritic cells in the small intestine.

IL23-fm tdTomato$^+$ cells were observed not merely in hematopoietic, but also in non-hematopoietic compartment (Figure 2). We next tried to identify anatomical location of these non-hematopoietic IL23-fm tdTomato$^+$ cells in the small intestine. Immunohistochemical staining for cryosection of the ileum show accumulation of IL23-fm tdTomato$^+$ cells in the muscle layer. As these tdTomato$^+$ cells were not co-stained with anti-CD11c antibody (Figure 3) nor with anti-CD45 antibody (data not shown), we speculate these intramuscular tdTomato$^+$ cells are part of CD45$^-$ IL23-fm tdTomato$^+$ cells observed in flow cytometry analysis.

Discussions

Despite of accumulated evidences that IL-23 plays central role on the development of autoimmune diseases and on the maintenance of intestinal barrier function, the actual cellular source of IL-23 in the intestine was still under debate. In the lamina propria of murine intestine, MNPs are sentinels, capable of responding to microbial products, and play a crucial role in orchestrating intestinal lymphocyte homeostasis. MNPs can be subdivided based on their expression of CD103 or CX_3CR_1 and each group has been ascribed critical functions in maintaining intestinal homeostasis. Among CD103$^+$ cells, which differentiate from common DC precursors, CD103$^+$CD11b$^+$ produce IL-23 in response to flagellin-induced Toll like Receptor (TLR) 5 activation, resulting in IL-22 production from ILC3 and has been proposed to support Th17 cells. In contrast to CD103$^+$ DCs, $CX_3CR_1^+$ MNPs differentiate from monocyte precursors. Longman et al. proved that $CX_3CR_1^+$ MNPs produce much higher level of IL-23 and IL-1□ than CD103$^+$ DCs in response to LPS and CPG DNA.

In this study, we succeeded in generating IL-23p19 reporter mice. Anatomical location of IL-23p19-expressed cells in the intestinal villi was consistent with that of $CX_3CR_1^+$ MNP that was previously reported by several groups. Flowcytometry analysis about surface molecules of IL-23p19-expressed cells also support the

previous result that $CX_3CR_1^+$ MNPs express IL-23p19. Our study also supports another evidence that IL-23p19 is expressed by $CX_3CR_1^-$ MNPs, presumable counter population of $CD103^+CD11b^+$ cells. More interestingly, in the intra-muscular region of the small intestine, there exist non-hematopoietic cells that have the history of IL-23p19 expression. These non-hematopoietic cells comprise of Auerbach's plexus that provides motor innervation to both layers of the muscular layer of the gut, having both parasympathetic and sympathetic input. To identify these intramuscular IL-23p19-expressed cells, more intensive study will be required.

Conclusion

In this study, we succeeded in establishing a new mouse model that enabled us to visualize IL-23p19-expresed cells in vivo. This mouse model is quite useful to understand anatomical relationship between MNPs and T cell or MNP and ILC3 *in vivo*. Moreover, unexpectedly found IL-23-expresed cells in Auerbach's plexus might provide us new research dimension in the field of neuro-immune biology.

Figure legends

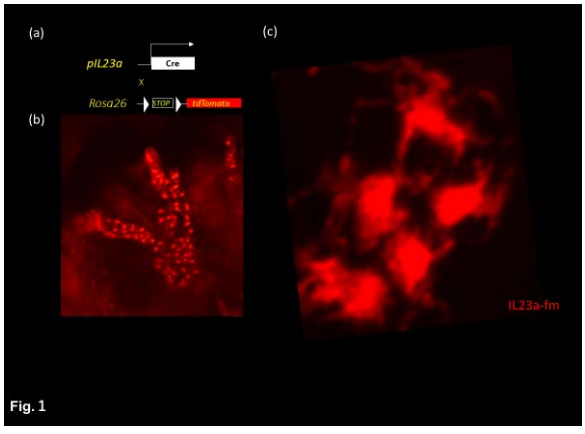

Fig. 1

Microscopic analysis of IL-23p19-expresed cells in IL23a-CIG BAC^{Tg};R26-tdTomato-LSL mice. (a) Scheme of tdTomato expression in IL23a-CIG BAC^{Tg};R26-tdTomato-LSL mice. (b)

Stereomicroscopic analysis of IL-23p19-expressed tdTomato cell in the small intestinal. (c) Confocal microscopic analysis of IL-23p19-expressed tdTomato cell in the villi.

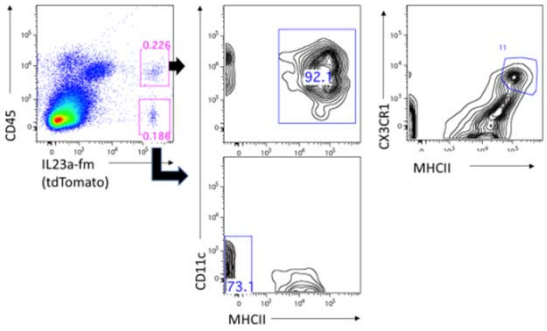

Fig. 2

Fig.2

Flowcytometry analysis about small intestinal cells of IL23a-CIG BAC^{Tg};R26-tdTomato-LSL mouse。IL-23p19-expressed tdTomat^{+} cells are composed of both CD45^{+} and CD45^{-} cells (upper left)。Most of CD45^{+} tdTomat^{+} cells are MHC class II^{+}CD11c^{+}DCs（upper middle）. Small fraction of tdTomato^{+} DCs express CX_3CR_1（upper right)。

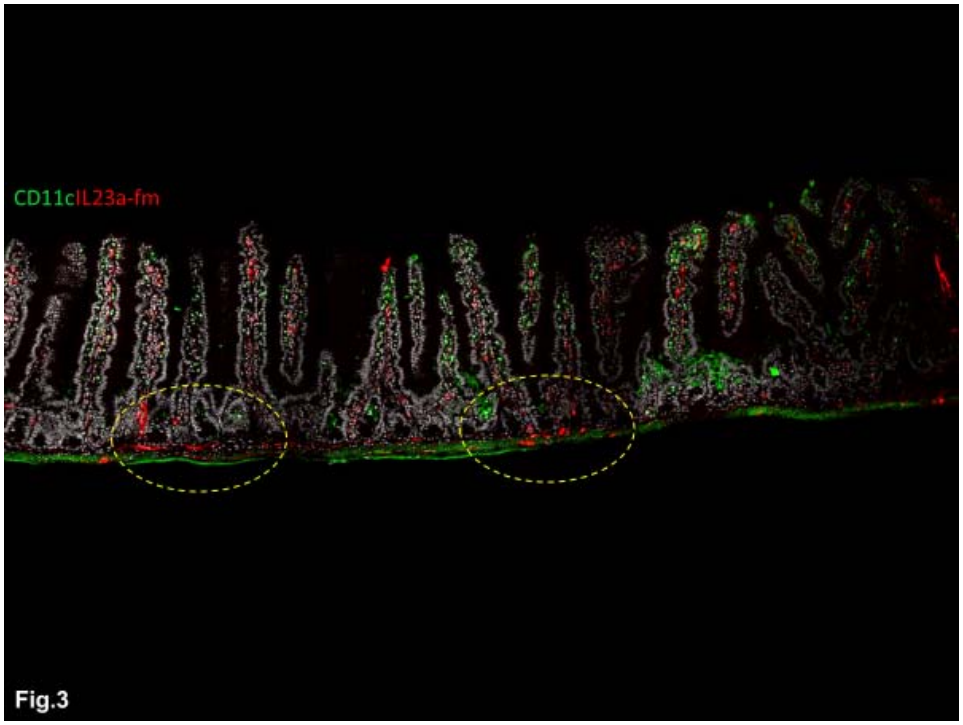

Fig. 3

Immunohistological analysis about cryosection of the small intestine obtained from IL23a-CIG BAC^{Tg};R26-tdTomato-LSL mouse. tdTomato^{+}CD11c^{-} cells in the intramuscular layer was highlighted with yellow dash circles. CD11c is indicated in green.

Establishment of immortalized Bonin flying fox (*Pteropus pselaphon*) derived cell and its application to the in vitro virus infection model

Tomokazu Fukuda

Graduate School of Science and Engineering, Iwate University, 4-3-5, Ueda, Morioka, Iwate, 020-8551, Japan

ABSTRACT

The mega bats are natural carrier of various emerging viruses, such as Ebola hemorrhagic fever and Lassa fever. The Bonin flying fox (*Pteropus pselaphon*) is one of the mega bats in Japan, which is known as one of the most critically endangered animals. The estimated number of this species would be around 150, and classified as the top rank of the international union of animal conservation. We established the primary cells from Bonin fling fox, and introduced the expression cassette, which expresses the human derived mutant Cyclin dependent kinase 4 (CDK4), Cyclin D, telomerase reverse transcriptase (TERT). Our research group previously showed that expression of CDK4, Cylcin D, and TERT efficiently induced the cellular immortalization with intact chromosome condition and original nature in human, bovine, swine, monkey, and buffalo derived cells. In this study, we successfully introduced CDK4, Cyclin D, and TERT into the primary cells derived from Bonin flying fox. The established cells showed efficient expression of introduced genes at protein level. Furthermore, the introduced cells showed no characteristics of cellular senescence, indicating our established Bonin flying fox derived cells reaches into the cellular immortalization. Since the established cells can be shared with the world wide scientists, and this cell would be useful *in vitro* tool for the infectious viruses which mediated by mega-bats.

INTRODUCTION

The Bonin flying fox (*Pteropus pselaphon*) is the original species in North and South Iwo Jima, that are part of Bonin Islands of Japan. During world war II, Bonin flying fox was hunted as the food, exported as military food to Guam island. Due to the hunting of human for food purpose, and forest destruction by human activity, the number of Bonin flying fox dramatically decreased around early part of 1970's. Bonin flying fox was believed to reach to extinct, since there was no report for the evidence of survival. However, in 1986, a colony of Bonin flying fox was found in a cave of Chichijima, which is one of Bonin Islands. As the results of protection and conservation activity, Bonin flying fox was nominated as Natural monument of Japan in 1969, and classified as endangered original species of Japan in 2009. Furthermore, Bonin flying fox was classified as a most critically endangered animal, which is highest risk to extinction in the International Union for Conservation of Nature (IUCN). The estimated individual number of Bonin flying fox is estimated around 130-150. From these situations, Bonin flying fox can be classified into the one of the most critically endangered animals.

In our previous studies, we showed that the expression of mutant Cyclin Dependent Kinase (CDK4) and Cyclin D, which is the binding partner of CDK4, and enzymatic subunit of telomerase (TERT) allows us to efficiently establish the immortalized cells in multiple species (1–8). Since the amino acid sequence of CDK4 and Cyclin D are conservative in the process of animal evolution from yeast to human, this immortalization method might be applied into the wide variety of species. Furthermore, the function of p53, which is one of the important gate keeping genes to maintain the intact genome, is still intact in these cell lines, and we reported that the immortalized cells with this method keeps original chromosome pattern, and original nature of primary cells (3). Since the chromosome condition is intact, the re-generation of Bonin flying fox itself might be possible after the applying the somatic cloning technique to our immortalized cells.

To be noted, the primary cells reaches into the cellular senescence after the certain times of cell division, resulting in the halt of the cell proliferation. In the process of the cellular senescence, p16 protein is known to accumulate in the cells. The p16 protein would bind to the specific

site of CDK4, and down regulate the enzymatic activity of protein complex of CDK4-Cyclin D. Inactivation of CDK4-Cyclin D complex results in the phosphorylation of Retinoblastoma protein (RB), which is an important gate keeper of cell cycle. From these situations, the primary cells can be classified as the limited resource. In this study, we built the hypothesis that the expression of mutant CDK4 and Cyclin D, and TERT might allow us to establish the immortalized cells of Bonin flying fox. As far as we know, we have not observed any previous study which report the establish the mega bats derived cell lines. From the view point of virus infection study, the mega bats is the key species for the expansion of the Emerging Viruses, such as Ebola hemorrhagic fever and Lassa fever virus. The mega bats are classified as potential host animal to expand the virus infection, we do not know the exact reason why the mega bats can be transmit these viruses in the field. The establishment of mega bats derived cell would contribute to understand the mechanism how the mega bats becomes virus carrier in the infection cycle.

METRIALS AND METHODS

Primary cells of Bonin flying fox

The muscle tissue of male Bonin flying fox was obtained from dead animal found at Ogasawara islands in 2008. The primary cells were established from its tissues in National Institute of Environmental Health Studies, NIES, Tsukuba, Japan. The primary cells were expanded in the DMEM/F12 medium (Wako Chemical, Osaka, Japan) containing 10% Fetal Bovine Serum (FBS) and 1 X antibody mixture (Nakarai Tesque, Kyoto, Japan). The expanded cells were preserved under the liquid nitrogen tank with 10% Dimethyl sulfoxide (DMSO) medium. Since the cells were established from the dead animals, our study is not restricted any regulation related to animal welfare and experiments, and animal conservation of endangered animals.

Preparation of recombinant retrovirus for the cellular immortalization

The protein-coding region of Cyclin Dependent Kinase 4 (CDK4) with R24C mutation, Cyclin D, and EGFP was chemically synthesized with Kozak sequence

and restriction enzyme sites. The insert cDNA was inserted into the multiple cloning site of pQCXIN vector with the restriction enzyme cutting, and following ligation reaction. The structure of recombinant retrovirus was shown in Figure 1A. After the G418 selection, the resistant recombinant cells were selected. At the same time, as the positive control of retrovirus infection, we infected QCXIN-EGFP, which expresses Enhanced Green Fluorescence Protein. Then, the retrovirus expressing the human derived telomere reverse transcriptase (TERT, pCLXSH-Acc TERT) was introduced by the infection. The infected cells were selected with G418 and Hygromycin, to ensure the expression of CDK4R24C mutant, Cyclin D, and TERT. From these sequential introductions, we named cells as wild type, EGFP (QCXIN-EGFP infected cell), K4D (mutant CDK4, Cyclin D expressing cell), K4DT (mutant CDK4, Cyclin D, and TERT expressing cell).

Western blot analysis and detection of telomerase activity with stretch PCR assay

The detailed method for the western blot detection and stretch PCR assay were described in our previous publications (3,4). In brief, Primary antibodies used in this study are listed in below. Antibody against Cyclin D (1:5000, code no. 553, MBL, Nagoya, Japan), CDK4 (1:2500, code no. K0065-3, MBL) and alpha-tubulin (1:1000, cat. no. sc-32293, Santa Cruz Biotechnology, Dallas, TX, USA) were used. Secondary antibodies used in this study are listed in below. Sheep anti-mouse IgG linked horseradish peroxidase (HRP) (1:2000, code no. NA931 V, GE Healthcare, Little Chalfont, UK) and a donkey anti-rabbit IgG linked HRP (1:2000, code no.NA934 V, GE Healthcare). Enzymatic activity of the telomere elongation was detected with commercially distributed kit 'TeloChaser' (code no. TLK-101, TOYOBO, Osaka, Japan). The detection procedure was performed by using the protocol provided by the manufacture.

Population doubling (PD) assay

Wild type, K4D and K4DT cell of Bonin flying were applied into the population-doubling assay. We carried out the sequential passages to evaluate the cell growth of wild type and recombinant cells, and evaluated with PD value, which

represents the number of cell divisions, which is calculated using the following formula; PD = $\log_2$ (a/b) where "a" is the number of cells counted at each passage and "b" is the number of cells seeded at the start of each passage (Qin et al. 2012). To obtain the value of "a", cells were seeded at a concentration of 5×10^4 cells/well (the value of "b") in a 6-well plate. When one of the cells in the wells reached confluence, all the cells from the plate were passaged and the number of cells in each well (the value of "a") was counted at the same time. Results are shown as the mean with standard deviation, from the experiment performed in triplicate.

RESULTS

The retrovirus can efficiently introduce into Bonin flying fox cells, but lentivirus does not.

In our previous study, we introduced mutant CDK4, Cylclin D, and TERT through the mixture and triple infection of monocistronic lentiviruses for cellular immortalization (1,2,4,6,8). At the first step, EGFP expressing lentivirus was applied to the primary Bonin flying fox derived cells. Surprisingly, even after the 48 hours of infection, very limited number of cell population showed EGFP expression, indicating that lentivirus is not efficient method for the introduction of exogenous genes (Figure 1C). From these reasons, we concluded that lentivirus is not suitable method for the efficient delivery of gene introduction.

We next selected retrovirus with VSV-G envelope. Interestingly, EGFP expressing retrovirus with VSV-G envelope protein showed around 10-20% efficiency for gene introduction. For the efficient establishment of immortalized cells, triple infection of monocistronic recombinant viruses is required, and infection efficiency around 10-20% of efficiency is not enough high, since the multiple infections of mutant CDK4, Cyclin D, and TERT is required for the immortalization. From this reason, we designed the polycistronic retrovirus, which expresses both of mutant CDK4 and Cyclin D. As shown in Figure 1A, large fusion protein, consisted with mutant CDK4, Cyclin D, Enhanced green Fluorescence Protein (EGFP) would be initially translated. Then, due to the existence of self cleavage 2A peptide between mutant CDK4, Cyclin D, and EGFP, three proteins would be rapidly separated into three independent proteins, based on the protease activity. Due to the existence of Internal Ribosomal Entry Site (IRES)-Neo resistant gene at the

downstream of the CDK4, Cyclin D, and EGFP, the selection with 1mg/ml of G418 in the cultured medium ensure the introduction of mutant CDK4 and Cyclin D, and EGFP in Bonin flying fox cells, and we named the cells as "K4D cells" (mutant CDK4 and Cyclin D introduced cells, Figure 1B). We confirmed that wild type Bonin flying fox derived cells couldn't survive at the existence of 1mg/ml of G418 (Data not shown). After the G418 selection, almost of all resistant cells showed the expression of EGFP, which result was expected from the structure of the expression system (Figure 1B). The cells were further infected with recombinant retrovirus, which encodes the enzymatic subunit of telomerase reverse transcriptase (TERT), and hygromycin resistant gene. The double infected cells were selected with hygromycin and G418 in cultured medium, which ensure the introduction of both of expression cassettes (mutant CDK4-Cyclin D-EGFP cassette, and TERT cassette). The established cells, which have mutant CDK4, Cyclin D, and TERT were named as "K4DT cells" (mutant CDK4, Cyclin D, and TERT expressing cells).

Detection of introduced protein with western blot analysis

To ensure the introduction of expression cassette of mutant CDK4, and Cyclin D, we carried out the detection of protein expression in wild type, K4D, and K4DT. As expected, expressions of CDK4 and Cyclin D were detected in expected combination at protein level. Furthermore, the enzymatic elongation activity of telomere sequence was detected by stretch PCR assay. As expected, K4DT cells showed positive for the extension activity due to the expression of TERT (Figure 2B).

Population doubling assay of wild type, K4D, and K4DT cells

Wild type, and K4D, and K4DT cells were applied to the sequential population-doubling assay. The results of the assay were shown in Figure 2C. Wild type cell showed the slow down of the cell proliferation speed from around passage 6. Interestingly, K4D cell and wild type cells showed slowdown of the proliferation, and positive staining for senescence associated

beta-galactosidase staining. While wild type and K4D cells showed decreased cell proliferation up to passage 6, K4DT cell continued cell proliferation and negative for senescence associated beta-galactosidase staining. From these situations, we concluded that Bonin flying fox derived K4DT cell is free from the cellular senescence, and successfully immortalized.
in case of critically

DISCUSSION

We previously showed that the expression of mutant CDK4 and Cylcin D, and TERT allows us to efficiently establish the immortalized cells in various species. In human, bovine, pig, monkey, midget buffalo, and prairie vole, wild cat derived cells showed the cellular immortalization with the combination of these three genes. However, interestingly, African derived elephant derived cell showed cellular senescence even after the introduction of these three genes. We do not know anything about the mega bat derived cells. Based on our data, we concluded that expression of mutant CDK4, Cyclin D, and TERT enable us to establish the mega bat derived cells. In addition to the male mega bat in this experiment, we also successfully established female other Ogasawara mega bat derived cells, indicating that immortalization with expression of mutant CDK4, Cyclin D and TERT is possible in Bonin flying fox bat derived cells.

As far as my understanding, this is the first reports which showed that successful establishment of immortalized cells from mega bats. Since the immortalized cell can proliferate infinite, the established cell can be distributed worldwide scientists. Even

in case of critically endangered species, the immortalized cell can be used as research materials since the established cell continues cell proliferation.

In previous studies in Low land anoa, and Tsushima leopard cat, K4D cell continued cell proliferation even after the wild type cell stop the cell proliferation. Interestingly, in case of Bonin flying fox bat, the K4D and wild type cells stopped cell proliferation almost same passage number. The stop of cell proliferation of K4D cell might be explained by the cellular stress during the sequential passages. Furthermore, the expression level of introduced genes might be different which depend on the cell and tissue type. For example, the protein

expression level of poly-cistronic CDK4-2A-Cyclin D-2A-EGFP cassette in Bonin flying fox derived cell was much lower when it compared with human corneal epithelial cells (data not shown). The fluorescence intensity which detected by EGFP fragment at the carboxyl terminus end of the expression cassette was much lower in Bonin flying fox derived cell. The different protein expression level in different cell type might be explained by cell specificity of the cytomegalovirus derived promoter activity. When the expression level becomes much higher with stronger promoter, such as CAG, cytomegalovirus derived promoter with first intron of chicken beta-actin and splice acceptor of rabbit beta-globin gene, the proliferation activity of Bonin flying fox derived cell might be accelerated.

CONCLUSION

In this study, we successfully established the immortalized cells from Bonin flying fox bat, and showed immortalized cells are useful material for the infectious studies and critically endangered animals.

FIGURE LEGENDS

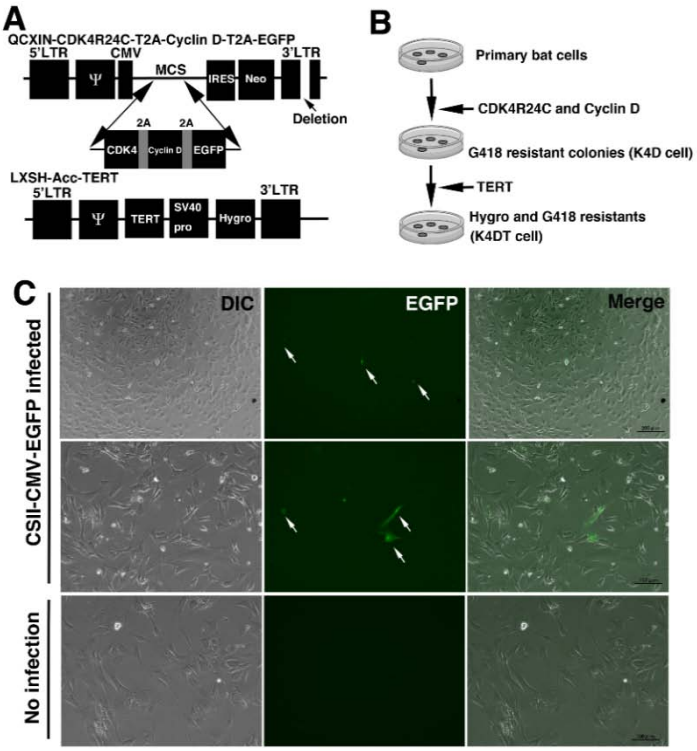

Figure 1. Structure of expression cassette and strategy for establishment of Bonin flying fox derived cells by the expression of mutant CDK4, Cyclin D, and telomerase reverse transcriptase. A, Schematic representation of recombinant lenti and retroviruses, which used for the immortalization. B, Schematic representation of strategy to obtain K4D and K4DT cells of Bonin flying fox derived cells. C, Genetic introduction of enhanced green fluorescence protein (EGFP) expressing lentivirus into Bonin flying fox derived cells. DIC, difference in contrast, EGFP, fluorescence detection of enhanced green fluorescence protein. Merge, merged picture of images.

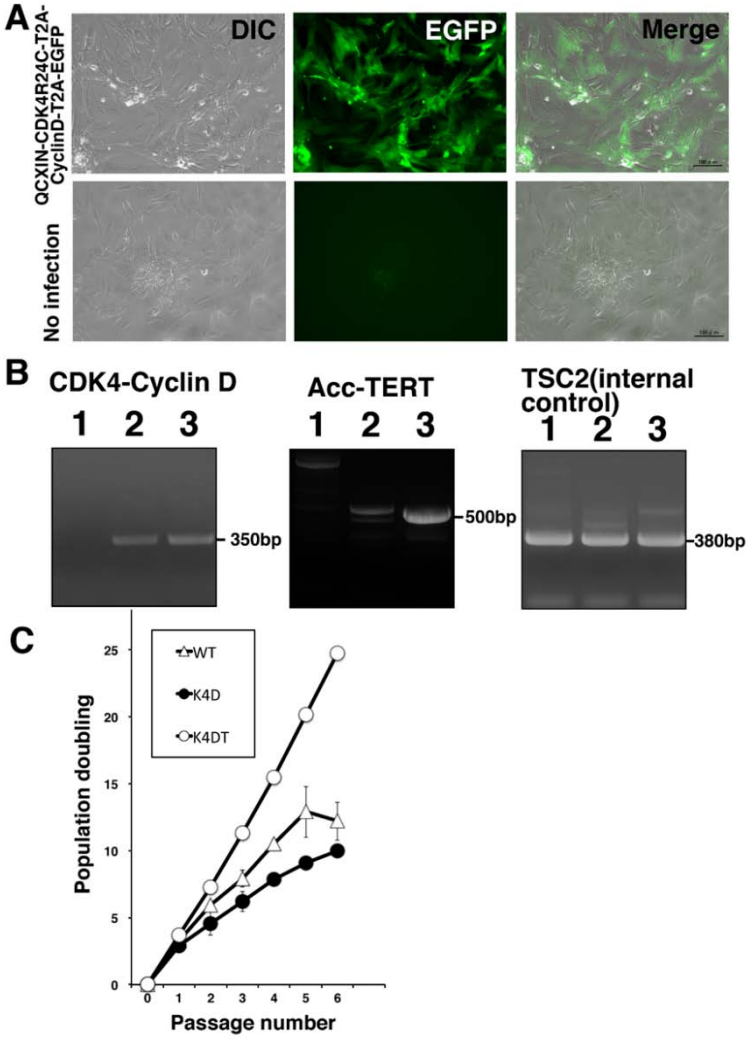

Figure 2. Fluorescence detection of Bonin flying fox derived cells after the G418 selection, and its biological characterization. A, Detection of EGFP derived fluorescence after the introduction of mutant CDK4, Cyclin D, and EGFP expressing retrovirus. B, Detection of genomic integrations of CDK4-Cyclin D expressing cassette in host cell, and TERT expressing retrovirus with PCR analysis. Amplification products from bat derived tuberous sclerosis type II (TSC2) was used as internal control. C, Results of sequential passages of wild type, K4D, and K4DT cell of Bonin flying fox derived cells. The results from triplicated samples were plotted.

REFERENCES

1. Donai K, Kiyono T, Eitsuka T, Guo Y, Kuroda K, Sone H, et al. Bovine and porcine fibroblasts can be immortalized with intact karyotype by the expression of mutant cyclin dependent kinase 4, cyclin D, and telomerase. J Biotechnol. 2014;176(1):50–7.

2. Kuroda K, Kiyono T, Isogai E, Masuda M, Narita M, Okuno K, et al. Immortalization of Fetal Bovine Colon Epithelial Cells by Expression of Human Cyclin D1, Mutant Cyclin Dependent Kinase 4, and Telomerase Reverse Transcriptase: An In Vitro Model for Bacterial Infection. Saretzki G, editor. PLoS One [Internet]. 2015 Dec 1 [cited 2018 Jun 17];10(12):e0143473. Available from: http://www.ncbi.nlm.nih.gov/pubmed/26624883

3. Fukuda T, Eitsuka T, Donai K, Kurita M, Saito T, Okamoto H, et al. Expression of human mutant cyclin dependent kinase 4, Cyclin D and telomerase extends the life span but does not immortalize fibroblasts http://www.ncbi.nlm.nih.gov/pubmed/25187009

6. Katayama M, Kiyono T, Horie K, Hirayama T, Eitsuka T, Kuroda K, et al. Establishment of an immortalized cell line derived from the prairie vole via

7. Katayama M, Hirayama T, Kiyono T, derived from loggerhead sea turtle (Caretta caretta). Sci Rep [Internet]. 2018 Jun 20 [cited 2018 Aug 19];8(1):9229. Available from: http://www.nature.com/articles/s41598-018-27271-x

4. Fukuda T, Iino Y, Eitsuka T, Onuma M, Katayama M, Murata K, et al. Cellular conservation of endangered midget buffalo (Lowland Anoa, Bubalus quarlesi) by establishment of primary cultured cell, and its immortalization with expression of cell cycle regulators. Cytotechnology [Internet]. 2016;68(5):1937–47. Available from: https://www.ncbi.nlm.nih.gov/pubmed/27449922

5. Kuroda K, Kiyono T, Eitsuka T, Isogai H, Takahashi K, Donai K, et al. Establishment of cell lines derived from the genus macaca through controlled expression of cell cycle regulators. J Cell Biochem [Internet]. 2015;116(2):205–11. Available from:

lentivirus-mediated transduction of mutant cyclin-dependent kinase 4, cyclin D, and telomerase reverse transcriptase. Exp Anim [Internet]. 2016;65(1):87–96. Available from: http://www.ncbi.nlm.nih.gov/pubmed/26496927

Onuma M, Tani T, Takeda S, et al.

Immortalized prairie vole-derived fibroblasts (VMF-K4DTs) can be transformed into pluripotent stem cells and provide a useful tool with which to determine optimal reprogramming conditions. J Reprod Dev [Internet]. 2017 Jun 21 [cited 2018 Aug 18];63(3):311–8. Available from: https://www.jstage.jst.go.jp/article/jrd/63/3/63_2016-164/_article

8. Gouko R, Onuma M, Eitsuka T, Katayama M, Takahashi K, Nakagawa K, et al. Efficient immortalization of cells derived from critically endangered Tsushima leopard cat (Prionailurus bengalensis euptilurus) with expression of mutant CDK4, Cyclin D1, and telomerase reverse transcriptase. Cytotechnology. 2018;in press.

Development of the method to predict adverse reaction caused by vaccination

Hiroyuki Oshiumi

Department of Immunology, Faculty of Life Sciences, Graduate School of Medical Sciences, Kumamoto University,1-1-1, Honjo, Chuo-ku, Kumamoto 860-8556 Japan

Introduction

Extracellular vesicles (EVs), including exosomes and microvesicles, deliver functional proteins and RNA from donor to recipient cells, thereby mediating intercellular communications [1, 2]. Exosomes are small vesicles released from multivesicular bodies, whereas microvesicles are released from the plasma membrane and have larger diameters than exosomes [3]. Sumoylated hnRNPA2B1 proteins recognize a motif called EXOmotif in microRNAs (miRNAs) and sort them to the exosomes [4]. There are several other mechanisms by which miRNAs are specifically sorted into the exosomes [5-8]. miRNAs can be sorted into microvesicles, although underlying mechanisms are unclear [9]. A variety of cell types take up miRNA-containing EVs, and the miRNAs are delivered into the cytoplasm, where they attenuate the functions of targeted mRNAs [10-12].

EVs can affect inflammations via miRNAs. miR-155-containing exosomes have been shown to promote the endotoxin-induced pro-inflammatory cytokine expression in dendritic cells, whereas miR-146a-containing exosomes have been shown to reduce the cytokine expression [12]. miR-451a is known to suppress pro-inflammatory cytokine expression following influenza A virus infection [13]. Recently, we showed that miR-451a in EVs suppresses the pro-inflammatory cytokine expression in macrophages after stimulation with influenza A virus vaccines [14]. Macrophages and dendritic cells efficiently uptake miRNAs in serum EVs, and internalized miR-451a in the cytoplasm targets 14-3-3ζ mRNA and reduces protein levels [14]. 14-3-3ζ is well known to be

required for pro-inflammatory cytokine expression [15]. Thus, miR-451a levels in serum EVs were negatively correlated to the expression levels of pro-inflammatory cytokines [14]. There are many other immune-regulatory miRNAs; however, the role of the EVs containing immune-regulatory miRNAs has not yet been fully elucidated [16].

Pro-inflammatory cytokines, such as IL-1β, IL-6, and TNF-α, cause local inflammation. TNF-α stimulates endothelial cells and increases the permeability of the blood vessels, which can cause pain, itching, swelling, and redness [17-20]. IL-1β, IL-6, and TNF-α function as endogenous pyrogens, leading to increased body temperature [18, 19]. Vaccination is the best prophylaxis for preventing infectious diseases; however, it sometimes causes the production of pro-inflammatory cytokines, and their excessive production leads to inflammation and thus local adverse reactions at the vaccination site [18, 19, 21]. Indeed, it has been shown that subjective symptoms, such as pain and swelling, at the vaccination site of the seasonal flu vaccine are correlated with the production of pro-inflammatory cytokines [22]. Because EV miR-451a reduces the production of pro-inflammatory cytokines [14], we hypothesized that circulating miR-451a levels within EVs might be inversely correlated with the strength of symptoms at the local site of the seasonal flu vaccine. In this study, we investigated the miRNA levels of circulating EVs before vaccination and compared them with local symptoms after flu vaccination, and found that miRNA levels in circulating EVs were correlated with the number of local symptoms after seasonal flu vaccination.

Materials and methods

Participants

Healthy Asian men and women between 22 and 62 years of age were recruited from the staff and faculty at Kumamoto University and its hospital during the 2018–2019 influenza season using a clinical research brochure. Those with any diseases or symptoms and pregnant women were excluded from the study. All participants provided written informed consent. This study was approved by the ethics committee of the Faculty of Life Sciences at Kumamoto University (RINRI 1524), and all experiments have been conducted according to the principles expressed in the Declaration of Helsinki.

Serum EV miRNA measurement

The serum of healthy subjects was collected 1–7 days before vaccination. EVs were collected from the sera using a Total Exosome Isolation Kit (from serum) (Thermo Fisher) according to the manufacturer's instruction. Total RNA of the collected EVs was extracted using TRIZOL reagent (Thermo Fisher). miRNAs were reverse transcribed using a MirX miRNA First-Strand Synthesis Kit (Clontech). Quantitative PCR was performed with the Power SYBR Green Master Mix (Thermo Fisher) on a Step One Real-Time PCR System (ABI). The levels of each miRNA were normalized to those of miR-16.

Measurement of subjective symptoms

Participants were vaccinated with the influenza HA vaccine (Kitasato Daiichi Sankyo Vaccine), 1 ml of which contained over 30 μg of the HA protein of each of the following four virus strains: A/Singapore/GP1908/2015 (H1N1) pdm09, A/Singapore/INFIMH-16-0019/2016 (H3N2), B/Phuket/3073/2013, and B/Maryland/15/2016. Subjective symptoms were counted based on a questionnaire completed by the subjects within 7 days of vaccination. The questionnaire inquired about the existence of subjective symptoms such as pain, itching, swelling, and redness at the vaccination site or a fever over 37 °C or 38 °C. In this study, no participants had a fever.

Statistical analyses

Pearson correlation coefficients were calculated using Prism 7 for Mac OS X. To investigate the statistical significance of miRNA expression levels between subjects with one or no symptoms and those with multiple symptoms, non-parametric analyses were performed using Prism 7 for Mac OS X software (Mann-Whitney U test, n = 33). Power values were calculated using the G*Power software (two-tailed).

Microarray analysis

A secondary analysis was performed on the data from the study by Okamoto M et al [14]. The accession number of the original data is GSE100128. The average levels of each miRNA were calculated using MS Excel software

Results

Negative correlation of miR-451a levels with the number of local symptoms after vaccination

To reveal the miRNA expression profile of circulating EVs, total RNA was extracted from EVs collected from human sera, and the expression profiles of miRNAs were investigated via microarray analysis. Fig 1A shows the top 20 highly expressed miRNAs in circulating EVs, of which miR-451a was the second most highly expressed. miR-451a is an immune suppressive miRNA, which targets 14-3-3ζ and attenuates pro-inflammatory cytokine expression [13]. Previously, we reported that miR-451a levels in circulating EVs were negatively correlated with the expression levels of pro-inflammatory cytokines [14]. Since the expression of pro-inflammatory cytokines corresponds with local symptoms after flu vaccination [22], we expected that miR-451a levels in circulating EVs would negatively correlates with the local symptoms.

To investigate the correlation between serum EV miR-451a levels and local subjective symptoms after vaccination, serum EVs were collected from healthy subjects 1–7 days before vaccination, because serum EV miR-451a levels are very stable for a week [14]. The concentrations of EVs ranged between 10^{12} and 10^{13} particles/ml (n = 33) (Fig 1B). Total RNA was extracted from the collected EVs, and miR-451a levels were determined by RT-qPCR and normalized to miR-16 levels, as described previously [14]. The normalized miR-451a levels showed a difference of over 10-fold (Fig 1C).

The healthy subjects were vaccinated with the HA seasonal flu vaccine, and the existence of subjective symptoms, such as pain, itching, swelling, redness, and fever were recorded based on questionnaires submitted by the subjects within a week of vaccination. Table 1 shows the number of healthy subjects with or without each symptom and their average serum EV miR-451a levels. Although pain, itching, swelling, and/or redness were observed in several subjects, no one had a fever after vaccination (Table 1). There was no significant difference between average miR-451a levels of subjects with and without symptoms of pain, itching, swelling, and redness (Table 1).

The subjects were divided into five groups based on their number of symptoms, and the miR-451a levels of each group are shown in Fig 1D. Interestingly, the miR-451a levels generally decreased as the number of symptoms increased (Fig 1D). Since severe inflammation was expected to

cause multiple symptoms, miR-451a levels were compared in subjects with and without multiple symptoms. The miR-451a levels of the multiple symptoms group were significantly lower than those of the one or no symptom group ($p < 0.05$, $n = 33$, Mann-Whitney U test) (Fig 1E). However, our power analysis revealed that the power value was less than 0.8; therefore, we could not exclude the possibility of a type 2 error. When the subjects were divided into groups based on their miR-451a levels, the number of the subjects with multiple symptoms decreased as miR-451a levels increased (Fig 1F).

Immune-regulatory miRNA expression in circulating EVs

To further identify miRNAs correlated with inflammation after vaccination, we focused on 20 immune-regulatory miRNAs [16]. Among the 20 immune-regulatory miRNAs, we could detect 12 miRNAs in serum EVs collected before vaccination (data not shown). The levels of each immune-regulatory miRNA in serum EVs showed a difference of over 10-fold as miR-451a levels did (data not shown).

To investigate whether those immune-regulatory miRNA levels are regulated independently, we compared the expression levels of the immune-regulatory miRNAs in the serum EVs with those of miR-451a (Fig 2A and Table 2). miR-23 levels were moderately correlated with miR-451a levels, and the correlation coefficient was 0.47, which was statistically significant ($p < 0.01$, power > 0.8) (Table 2). However, those of the other miRNAs did not exhibit any correlation with those of miR-451a (Fig 2A and Table 2). These data suggested that miR-451a expression levels in circulating EVs were distinct from most of other immune-regulatory miRNAs. Since the expression levels of other immune-regulatory miRNAs were different from those of miR-451a, we hypothesized that those miRNAs levels would independently affect excessive inflammation in response to vaccination.

Next, we investigated the correlation coefficient among the immune-regulatory miRNAs (Table 2). Several miRNAs exhibited strong correlation in their expression levels in circulating EVs. For instance, miR-204-3p levels were strongly correlated with those of miR-92a and miR-221, and a strong correlation was also observed between the expression levels of miR-23 and miR-30b (Fig 2B and Table 2). However, most of the other immune-regulatory miRNA levels were not

correlated with each other (Table 2). These data suggested that their expression was regulated independently, and we next investigated whether there were miRNAs in which their expression levels were correlated with the number of symptoms after vaccination.

Correlation of miRNA levels and the number of symptoms after vaccination

To identify immune-regulatory miRNAs whose expression were correlated with the number of symptoms after vaccination, the subjects were classified into five groups based on the number of symptoms, and the average levels of each miRNA were determined. We compared the average miRNA levels of each group with the number of symptoms as shown in Fig 3A. Interestingly, correlation coefficients of miR-451a, miR-29a, and miR-107 were below -0.70, suggesting that there are negative correlations between the number of symptoms and average of miRNA levels (Fig 3A). In contrast, only miR-22 exhibited a high positive correlation coefficient value (correlation coefficient = 0.52), suggesting that there was a positive correlation between average miRNA levels and the number of symptoms (Fig 3A).

Previous studies have reported that miR-29a and miR-107 exhibits anti-inflammatory effects like miR-451a, whereas miR-22 exhibits pro-inflammatory effects [16]. Therefore, we calculated normalized miRNA levels using miR-451a, miR-29a, miR-107, and miR-22 levels, in which miR-451a, miR-29a, and miR-107 levels were used as the numerators and miR-22 levels were used as the denominators, since the miR-22 exhibited the opposite trend to miR-451a miR-29a, and miR-107 trends. Because average levels of miR-22, 29a, and 107 were lower than those of miR-451a, each miRNA level was divided by each average miRNA level in the equation. The calculated normalized miRNA levels showed a difference of over 10-fold (Fig 3B).

Interestingly, the normalized miRNA levels clearly decreased as the number of symptoms increased (Fig 3B). In addition, the normalized miRNA levels of each subject with multiple symptoms were markedly lower than those of subjects with one or no symptoms (Fig 3C). This was consistent with our observation that miR-29a, miR-107, and miR-451a levels were negatively correlated with the number of symptoms; miR-22 levels were positively correlated with the number of symptoms (Fig 3B). Statistical analysis showed that this difference was significant

($p < 0.01$), with a power value greater than 0.8. Moreover, most of the healthy subjects with high calculated values (> 8) exhibited one or no symptoms (Fig 3D). Since sera were collected before vaccination, these data suggested that circulating miRNAs within EVs could be used as biomarkers for local symptoms after influenza vaccination.

Correlation of miRNA levels with the severity of mouse experimental autoimmune encephalomyelitis

Next, we investigated the correlation of circulating miRNA levels with other immune response. Mouse experimental autoimmune encephalomyelitis (EAE) is a model for multiple sclerosis and acute disseminated encephalomyelitis (ADEM). Since ADAM is a rare adverse reaction after human papilloma virus (HPV) vaccination, we investigated whether miRNA levels in circulating EVs are correlated to the severity of mouse EAE after HPV vaccination. Sera were collected from mouse tail vein, and EVs were isolated. miRNA levels in serum EVs were determined by RT-qPCR. 1 day later, mice were vaccinated with HPV vaccines and then injected with myelin oligodendrocyte glycoproteins, pertussis toxins, and adjuvants to induce mouse EAE. The EAE symptom of each mice were observed over 30 days. Interestingly, we found that some of the miRNA levels were clearly correlated with the severity of mouse EAE (data not shown). Collectively, our data indicate that miRNA levels in circulating EVs can be good biomarkers to predict the severity of excessive or abnormal immune response after vaccination.

Discussion

Excessive production of pro-inflammatory cytokines induces acute inflammation, increasing local blood flow via the activation of endothelial cells and increased vascular permeability and leading to swelling, redness, and pain [21]. A previous clinical study showed that the production of pro-inflammatory cytokines corresponded with the subjective symptoms after seasonal flu vaccination [22]. Recently, we showed that EVs deliver miR-451a into macrophages and dendritic cells [14]. miR-451a targets 14-3-3ζ and attenuates the production of pro-inflammatory cytokine expression. Interestingly, circulating miR-451a levels in EVs are correlated with those in macrophages and dendritic cells,

since EVs deliver miRNAs into those cells [3, 9, 14]. Therefore, it was expected that circulating EV miR-451a levels would be negatively correlated with pro-inflammatory cytokine production levels in response to vaccines. In this study, we compared circulating EV miR-451a levels and symptoms after seasonal flu vaccination. Interestingly, miR-451a levels in the circulating EVs of healthy subjects with multiple symptoms were significantly lower than those of subjects without multiple symptoms. Since severe inflammation is expected to cause multiple symptoms, our data indicated that the level of miR-451a in circulating EVs can be used to predict severe inflammation after vaccination.

EVs deliver the immune-regulatory miRNAs. Increased miR-451a levels affect the inflammatory responses of innate immune cells, such as macrophages and dendritic cells, thereby suppressing local inflammation. It is still possible that circulating EV miR-451a reflects the inflammatory state of healthy subjects. miR-451a-containing EVs are released from a variety of cell types as miR-451a contains an EXO-motif, which promotes the sorting of miRNAs into the exosomes. Several studies have reported that EV miR-451a levels are higher in patients with diseases. Therefore, we cannot exclude the possibility that some body conditions affect both circulating EV miR-451a levels and local inflammation after vaccination; thus, EV miR-451a levels appear to be correlated with symptoms after vaccination.

Although circulating EV miR-451a levels correlated with the local symptoms after vaccination, it is still unclear whether the levels are correlated with the efficacy of the vaccine. Considering that production of antigen-specific antibodies requires many types of immune cells, such as macrophages, dendritic cells, T cells, and B cells, it is possible that miR-451a levels are not sufficient to predict the efficacy of vaccination.

There are several other immune-regulatory miRNAs in circulating EVs, and we determined 12 miRNA levels in this study. The expression levels of serum EV miR-29a and miR-107 decreased as the number of symptoms increased, whereas those of miR-22 increased as the number of symptoms increased. Interestingly, the values calculated using the four miRNA levels were significantly lower in subjects with multiple symptoms than in those without multiple symptoms. miR-22, miR-29a, and miR-107 are involved in pro-inflammatory cytokine production pathways [16]. miR-107 downregulates mRNA of IL-12p19 mRNA [23], and miR-29a

decreases IL-6 and TNF-α mRNA [24]. miR-22 is known to increase pro-inflammatory cytokine expression in endothelial cells [25]. Although the underlying mechanisms remain unclear, these miRNAs might cooperatively regulate inflammation after vaccination. In addition, we found that miRNA levels were also correlated with the severity of mouse EAE after HPV vaccination. Overall, our data indicated that the miRNAs in circulating EVs could be potential biomarkers for predicting the risk of adverse reactions to vaccination. Fears of adverse reactions sometimes cause the reduction of vaccination rates. Our findings would be useful in understanding the mechanism governing adverse reactions of vaccinations, and we expect that this understanding may relieve the fears of adverse reaction, leading to increased vaccination rates.

Conclusion

EVs deliver immune regulatory miRNAs into myeloid and lymphoid cells. Fluctuation of miRNA levels in circulating EVs affect the immune response after vaccination. Our data indicate that miRNA levels in circulating EVs can be biomarkers to predict adverse reaction after vaccination.

References

1. Robbins PD, Morelli AE. Regulation of immune responses by extracellular vesicles. Nat Rev Immunol. 2014;14(3):195-208.

2. Simons M, Raposo G. Exosomes--vesicular carriers for intercellular communication. Curr Opin Cell Biol. 2009;21(4):575-81.

3. Colombo M, Raposo G, Thery C. Biogenesis, secretion, and intercellular interactions of exosomes and other extracellular vesicles. Annu Rev Cell Dev Biol. 2014;30:255-89.

4. Villarroya-Beltri C, Gutierrez-Vazquez C, Sanchez-Cabo F, Perez-Hemandez D, Vazquez J, Martin-Cofreces N, et al. Sumoylated hnRNPA2B1 controls the sorting of miRNAs into exosomes through binding to specific motifs. Nat Commun. 2013;4:2980.

5. Shurtleff MJ, Temoche-Diaz MM, Karfilis KV, Ri S, Schekman R. Y-box protein 1 is required to sort microRNAs into

exosomes in cells and in a cell-free reaction. Elife. 2016;5.

6. Santangelo L, Giurato G, Cicchini C, Montaldo C, Mancone C, Tarallo R, et al. The RNA-Binding Protein SYNCRIP Is a Component of the Hepatocyte Exosomal Machinery Controlling MicroRNA Sorting. Cell Rep. 2016;17(3):799-808.

7. Koppers-Lalic D, Hackenberg M, Bijnsdorp IV, van Eijndhoven MA, Sadek P, Sie D, et al. Nontemplated nucleotide additions distinguish the small RNA composition in cells from exosomes. Cell Rep. 2014;8(6):1649-58.

8. Cha DJ, Franklin JL, Dou Y, Liu Q, Higginbotham JN, Demory Beckler M, et al. KRAS-dependent sorting of miRNA to exosomes. Elife. 2015;4:e07197.

9. Kouwaki T, Okamoto M, Tsukamoto H, Fukushima Y, Oshiumi H. Extracellular Vesicles Deliver Host and Virus RNA and Regulate Innate Immune Response. Int J Mol Sci. 2017;18(3):666.

10. Valadi H, Ekstrom K, Bossios A, Sjostrand M, Lee JJ, Lotvall JO. Exosome-mediated transfer of mRNAs and microRNAs is a novel mechanism of genetic exchange between cells. Nat Cell Biol. 2007;9(6):654-9.

11. Kouwaki M, Fukushima Y, Daito T, Sanada T, Yamamoto N, Mifsud EJ, et al. Extracellular Vesicles Including Exosomes Regulate Innate Immune Responses to Hepatitis B Virus Infection. Frontiers in Immunology. 2016;7:335.

12. Alexander M, Hu R, Runtsch MC, et al. Exosome-delivered microRNAs modulate the inflammatory response to endotoxin. Nat Commun. 2015;6:7321.

13. Rosenberger CM, Podyminogin RL, Navarro G, Zhao GW, Askovich PS, Weiss MJ, et al. miR-451 regulates dendritic cell cytokine responses to influenza infection. J Immunol. 2012;189(12):5965-75.

14. Okamoto M, Fukushima Y, Kouwaki T, Daito T, Kohara M, Kida H, et al. MicroRNA-451a in extracellular, blood-resident vesicles attenuates macrophage and dendritic cell responses to influenza whole-virus vaccine. J Biol Chem. 2018;293(48):18585-600.

15. Pan X, Wang R, Wang ZX. The potential role of miR-451 in cancer diagnosis, prognosis, and therapy. Mol Cancer Ther. 2013;12(7):1153-62.

16. Smyth LA, Boardman DA, Tung SL, Lechler R, Lombardi G. MicroRNAs affect dendritic cell function and phenotype. Immunology. 2015;144(2):197-205.

17. Vandenbroucke E, Mehta D, Minshall R, Malik AB. Regulation of endothelial junctional permeability. Ann N Y Acad Sci. 2008;1123:134-45.

18. Dinarello CA. Infection, fever, and

exogenous and endogenous pyrogens: some concepts have changed. J Endotoxin Res. 2004;10(4):201-22.

19. Dinarello CA. Cytokines as endogenous pyrogens. J Infect Dis. 1999;179 Suppl 2:S294-304.

20. Kawabata A. Prostaglandin E2 and pain--an update. Biol Pharm Bull. responses correspond with subjective side effects after influenza virus vaccination. Vaccine. 2015;33(29):3360-6.

23. Xue X, Cao AT, Cao X, Yao S, Carlsen ED, Soong L, et al. Downregulation of microRNA-107 in intestinal CD11c(+) myeloid cells in response to microbiota and proinflammatory cytokines increases IL-23p19 expression. Eur J Immunol. 2014;44(3):673-82.

24. Chen T, Li Z, Tu J, Zhu W, Ge J, Zheng 2011;34(8):1170-3.

21. Pober JS, Sessa WC. Evolving functions of endothelial cells in inflammation. Nat Rev Immunol. 2007;7(10):803-15.

22. Christian LM, Porter K, Karlsson E, Schultz-Cherry S. Proinflammatory cytokine

X, et al. MicroRNA-29a regulates pro-inflammatory cytokine secretion and scavenger receptor expression by targeting LPL in oxLDL-stimulated dendritic cells. FEBS Lett. 2011;585(4):657-63.

25. Gu W, Zhan H, Zhou XY, Yao L, Yan M, Chen A, et al. MicroRNA-22 regulates inflammation and angiogenesis via targeting VE-cadherin. FEBS Lett. 2017;591(3):513-26.

Figure Legends

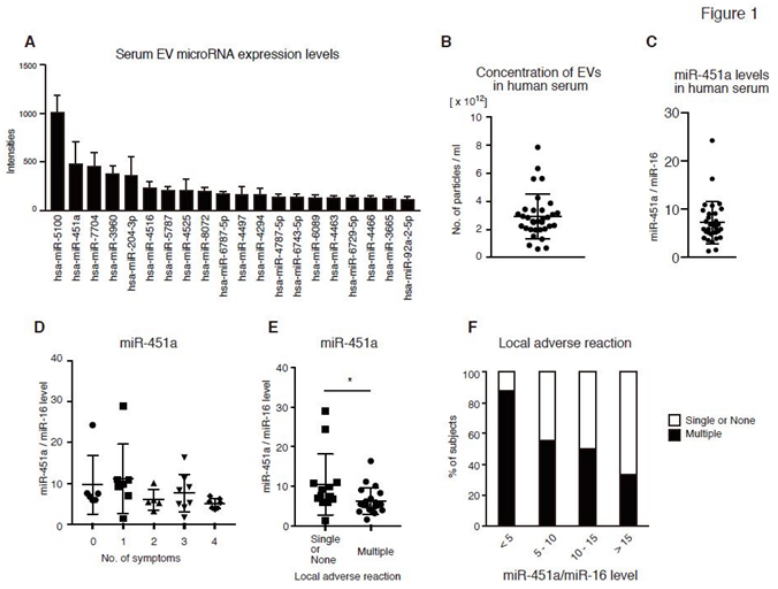

Fig 1. Correlation of miR-451a/miR-16 levels with local symptoms after vaccination.

(A) EVs were prepared from the sera of six healthy human subjects, and total RNA was extracted. miRNA expression profiles were determined via microarray analysis. The graph shows the top 20 highly expressed miRNA levels. Data represent the mean ± SD (n = 6).

(B, C) Sera were collected from 33 healthy subjects. The concentration of EVs in the sera was determined using a nanoparticle tracking analysis system (NanoSight) (B). miR-451a levels in serum EVs were determined using RT-qPCR and were normalized to those of miR-16 (C).

(D) miR-451a/miR-16 levels were determined before vaccination, and then 33 healthy subjects were vaccinated with the influenza A virus vaccine. Symptoms at the vaccination sites (pain, itching, redness, and swelling) that occurred within a week of vaccination, were counted. The subjects were divided into five groups based on their number of symptoms, and the miR-451a/miR-16 levels of each group are shown.

(E) The subjects were classified into the groups of those with one or no symptoms and those with multiple symptoms. The miR-451a/miR-16 levels in the two groups are shown.

(F) The subjects were classified into four groups based on their miR-451a/miR-16 levels as indicated. The percentages of the subjects with one or no symptoms (open box) and those with multiple symptoms (closed box) are shown.

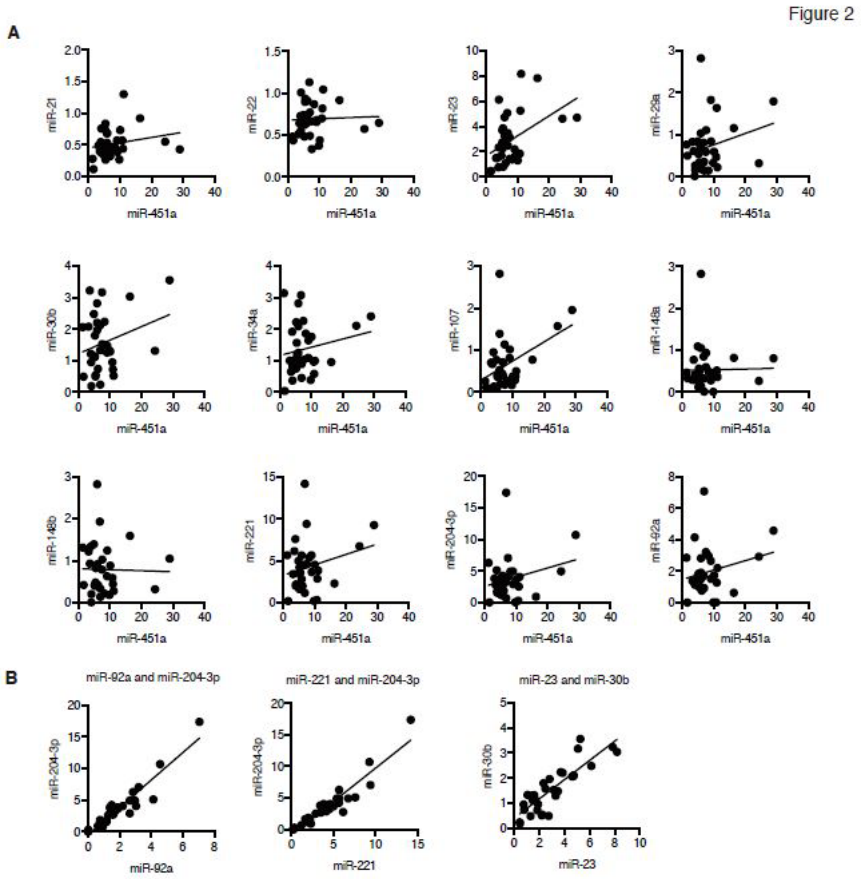

Fig 2. Concomitant expression of immune-regulatory miRNAs in circulating EVs

(A, B) Human sera were collected from 33 healthy subjects. Serum EV miRNA levels were determined by RT-qPCR and normalized to miR-16 levels. Correlations between the levels of miR-451a and other immune-regulatory miRNA levels were investigated (A). Strong correlations ($r > 0.8$) were observed among miR-92a, miR-204-3p, and miR-221, and between miR-23 and miR-30b (B). Correlation coefficients are described in Table 2.

Figure 3

A

	no. of symptoms	miR-451a	miR-21	miR-22	miR-23	miR-29a	miR-30b	miR-34a	miR-107	miR-148a	miR-148b	miR-221	miR-204-3p	miR-92a
Average (each group)	4	5.05	0.43	0.74	1.60	0.35	1.17	1.41	0.47	0.46	0.67	5.39	5.12	2.73
	3	7.58	0.62	0.79	3.94	0.69	1.76	1.05	0.54	0.53	0.71	4.25	3.19	1.78
	2	5.96	0.64	0.59	2.54	0.54	1.12	1.24	0.47	0.45	0.62	2.56	2.03	1.16
	1	11.13	0.40	0.60	2.75	0.86	1.48	1.06	0.70	0.36	0.70	2.99	2.99	1.38
	0	9.65	0.52	0.69	3.64	0.71	2.02	2.14	0.69	0.54	1.05	6.09	4.96	2.54
Average (Total)		7.93	0.52	0.69	2.92	0.64	1.53	1.36	0.58	0.47	0.75	4.30	3.70	1.94
Correlation coefficient		-0.80	0.05	0.52	-0.49	-0.73	-0.58	-0.52	-0.83	0.00	-0.69	-0.02	0.06	0.18

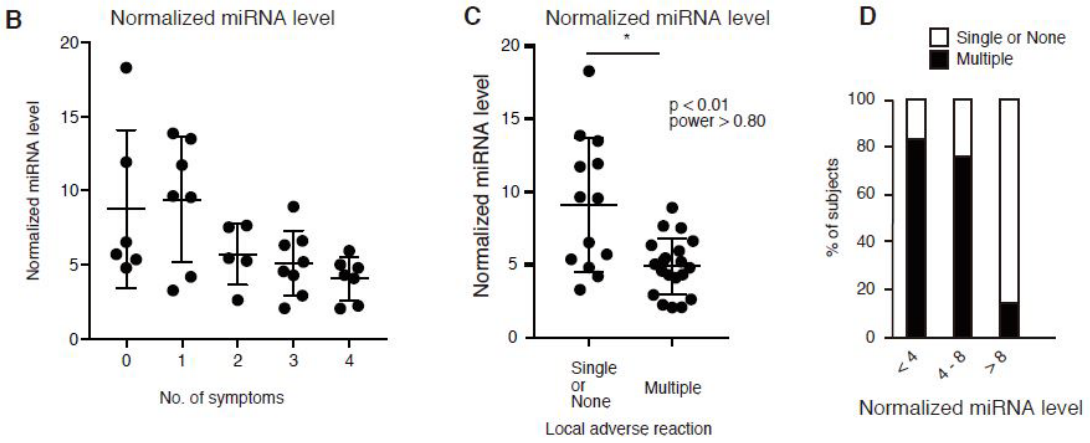

Fig 3. Correlation between miRNA levels and the number of local symptoms.

(A) Healthy subjects were classified into five groups based on the number of local symptoms after influenza vaccination. The averages of each miRNA level of each group and all subjects (total) were shown. Correlation coefficients between the number of symptoms and the average of each group were calculated.

(B) Normalized miRNA levels were calculated using the following equation: normalized miRNA level = (miR-451a/α + miR-29a/β + miR-107/γ) / miR-22/δ (B). The α, β, γ, and δ coefficients were the averages of each miRNA level, respectively, which were used because the averages for miR-29, miR-107, and miR-22 were very small compared to that of miR-451a. miR-22 levels were used as the denominators since miR-22 levels showed the opposite trend compared to miR-451a, miR-29a, and miR-107 levels.

(C) Healthy subjects were classified into two groups, those with one or no symptoms and those with multiple symptoms. The normalized miRNA levels of subjects with one or no symptoms and those with multiple symptoms are shown on the graph (*$p < 0.01$ (Mann-Whitney U test), power > 0.8).

(D) Healthy subjects were classified based on their normalized miRNA levels as indicated. The percentage of subjects with one or no symptoms (open box) and those with multiple symptoms (closed box) are shown on the graph.

Table 1. Summary of local adverse reactions after vaccination with HA split vaccine

Types of adverse reaction	Symptom	No of subjects	miR-451a/miR-16 level	
			mean	sd
Itching	Present	15	6.32	3.50
	Absent	18	9.26	6.71
Pain	Present	17	6.66	3.62
	Absent	16	9.27	7.24
Swelling	Present	20	7.13	9.15
	Absent	13	5.70	5.80
Redness	Present	17	6.48	3.68
	Absent	16	9.46	7.13
Fever	Present	0	*nd	*nd
	Absent	30	7.93	5.74

*nd: not determined

Table 2. Correlation coefficient (r) of miRNA levels in circulating EVs

	miR-451a	miR-21	miR-22	miR-23	miR-29a	miR-30b	miR-34a	miR-107	miR-148a	miR-148b	miR-221	miR-204-3p	miR-92a
miR-451a		0.21	0.04	*0.46	0.33	0.36	0.11	0.09	0.07	0.33	0.05	0.10	-0.02
miR-21			0.42	*0.67	0.36	*0.45	-0.06	0.18	*0.47	0.41	-0.01	-0.13	-0.20
miR-22				*0.52	0.37	*0.62	0.06	0.30	*0.49	0.32	0.44	0.35	0.29
miR-23					0.41	*0.86	0.32	0.37	*0.68	*0.69	0.23	0.09	0.03
miR-29a						0.41	0.13	0.42	*0.46	0.42	0.18	0.19	0.12
miR-30b							*0.45	*0.56	*0.61	*0.57	*0.49	0.36	0.30
miR-34a								0.44	0.39	*0.53	0.44	0.35	0.42
miR-107									0.35	0.31	*0.59	*0.48	*0.49
miR-148a										*0.61	0.25	0.15	0.18
miR-148b											0.22	0.09	0.13
miR-221												*0.94	*0.93
miR-204-3p													*0.94

*: statistically significant ($n = 33$, $p < 0.01$, power > 0.8)

Role of the multidrug efflux pump and its regulation in bacterial homeostasis

Kunihiko Nishino

Institute of Scientific and Industrial Research, Osaka University, 8-1 Mihogaoka, Ibaraki, Osaka 567-0047, Japan.

Abstract

During infection, *Salmonella* senses and responds to harsh environments within the host. Persistence in a bile-rich environment is important for *Salmonella* to infect the small intestine or gallbladder and the multidrug efflux system AcrAB-TolC is required for bile resistance. The genes encoding this system are mainly regulated by the *ramRA* locus, which is composed of the divergently transcribed *ramA* and *ramR* genes. The *acrAB* and *tolC* genes are transcriptionally activated by RamA, whose encoding gene is itself transcriptionally repressed by RamR. RamR recognizes multiple drugs; however, the identity of the environmental signals to which it responds is unclear. Here, we describe the crystal structures of RamR in complexes with bile components, including cholic acid and chenodeoxycholic acid, determined at resolutions of 2.0 and 1.8 Å, respectively. Both cholic and chenodeoxycholic acids form four hydrogen bonds with Tyr59, Thr85, Ser137 and Asp152 of RamR, instead of π–π interactions with Phe155, a residue that is important for the recognition of multiple compounds including berberine, crystal violet, dequalinium, ethidium bromide and rhodamine 6G. Binding of these compounds to RamR reduces its DNA-binding affinity, resulting in the increased transcription of *ramA* and *acrAB-tolC*. Our results reveal that *Salmonella* senses bile acid components through RamR and then upregulates the expression of RamA, which can lead to induction of *acrAB-tolC* expression with resulting tolerance to bile-rich environments.

Introduction

Salmonella is a bacterial pathogen that causes a variety of foodborne illnesses in humans. During the course of its infection of the intestinal tract and gallbladder,

Salmonella is exposed to bile acids. These are detergent-like biological substances that are synthesized in the liver from cholesterol and stored in the gallbladder. These bile acids possess strong antimicrobial activity, disrupt cell membranes, denature proteins and trigger DNA damage.[1,2] Enteric bacteria such as *Salmonella* must tolerate the presence of bile acids in order to survive in the gastrointestinal transit and gallbladder.[3,4] Enteric bacteria have developed an intrinsic resistance to the toxic effects of bile acids, due to the low permeability of their outer membranes to lipophilic solutes and the presence of active efflux mechanisms.[5,6]

Salmonella enterica serovar Typhimurium (*S.* Typhimurium) contains at least nine multidrug efflux systems.[7] Among these, the AcrAB-TolC system, whose AcrB transporter belongs to the resistance–nodulation–cell division family, is particularly effective in generating bile acid resistance.[7,8] Bile induces the expression of *acrAB*,[8] and this induction is mediated by the transcriptional regulators RamA and RamR.[9,10] The global transcriptional activator RamA, which belongs to the AraC/XylS family of regulatory proteins, activates the expression of *acrAB* and *tolC* genes.[9] The local transcriptional repressor RamR, which is located directly upstream of *ramA*, belongs to the TetR family of regulatory proteins and represses the expression of both *ramA* and *ramR* (Fig. 1a).[10,11] Additionally, it has recently been found that bile inhibits the binding of RamR to the *ramA* promoter region and activates *ramA* gene expression, resulting in the increased expression of *acrAB* and *tolC*.[10]

Our previous biochemical and structural studies found that RamR can recognize multiple compounds, including berberine, crystal violet, dequalinium, ethidium bromide and rhodamine 6G.[12] Binding of these compounds to RamR results in the increased expression of *ramA*; all the compounds recognized by RamR are also known substrates of AcrAB. However, these five drug compounds are not usually present in environments inhabited by *Salmonella*, such as the intestine, and so, because bile induces *ramA* expression, we hypothesized that RamR also recognizes some components of bile acids.[10]

There are several derivatives of bile acids. Two primary compounds, cholic (3α, 7α, 12α-trihydroxy-5β-cholan-24-oic acid; Fig. 1b) and chenodeoxycholic acids (3α, 7α-dihydroxy-5β-cholan-24-oic acid; Fig. 1b) belong to the C24 group, whose members have steroidal backbones and are metabolized from cholesterol in hepatocytes.

Primary bile acids are metabolized in the liver, via conjugation to glycine or taurine.[13] In the intestine, a broad range of intestinal anaerobic bacteria modify primary bile acids through hydrolysis and hydroxyl group dehydrogenation to produce secondary bile acids, such as deoxycholic acid (3α, 12αdihydroxy-5β-cholan-24-oic acid; Fig. 1b) and lithocholic acid (3α-hydroxy-5β-cholan-24-oic acid). Here, we report the crystal structure of RamR in complex with cholic and chenodeoxycholic acids. Both cholic and chenodeoxycholic acids decreased the DNA-binding affinity of RamR, resulting in increased transcription of *ramA*.

Results

Cholic and chenodeoxycholic acids induce *ramA* expression in a RamR-dependent manner

It has previously been shown that *ramA* expression is activated by a crude ox-bile extract, which is mainly dependent on RamR and is required for the bile-mediated transcriptional activation of *acrAB* and *tolC* genes.[10] However, the components of bile that influence the expression level of *ramA* have, to date, remained unknown. To identify these components and investigate their possible action on RamR, we tested the effect of a crude ox-bile extract, primary bile acids (cholic and chenodeoxycholic acids), and a secondary bile acid (deoxycholic acid) on the expression level of *ramA* in the wild-type *S.* Typhimurium strain and its *ramR* deletion mutant (Fig. 1c). We confirmed that the bile extract increased the *ramA* transcript level by approximately 20-fold in the wild-type strain, but by only by 3.9-fold in the *ramR* deletion mutant (Fig. 1c). Among the bile acid components tested, chenodeoxycholic and cholic acids increased *ramA* expression by more than 5.0-fold in the wild-type strain (7.2- and 5.6-fold, respectively; Fig. 1c), but not in the mutant (a 0.8-fold reduction and a 1.6-fold increase, respectively; Fig. 1c). These results indicate that *ramA* induction by cholic and chenodeoxycholic acids is dependent on RamR. In contrast, deoxycholic acid increased *ramA* expression only slightly; this effect appeared to be independent of RamR, as it was similar in the wild-type strain (1.7-fold increase) and in the *ramR* deletion mutant (2.7-fold increase)

Binding of bile acids to RamR

Because cholic and chenodeoxycholic acids induce *ramA* in a RamR-dependent manner, we hypothesized that these compounds are recognized by RamR. To test the possibility that cholic and chenodeoxycholic acids may bind to RamR, we employed surface plasmon resonance (SPR) analysis using a Biacore T200 instrument (GE Healthcare). Cholic and chenodeoxycholic acids were separately passed over RamR immobilized on a CM5 sensor chip and the SPR responses indicated that both bound directly to RamR, with the responses increasing in a concentration-dependent manner (Fig. 1d). The K_D values obtained from SPR data for chenodeoxycholic and cholic acids were 65.3 μM and 60.5 μM, respectively.

Co-crystal structures of RamR with cholic acid and chenodeoxycholic acid

To elucidate the recognition mechanism of cholic and chenodeoxycholic acids by RamR, we determined the individual crystal structures of RamR complexed to both of these compounds (Fig. 2a). Electron density maps of each co-crystal structure are shown in Figure 2b and these structures were refined to resolutions of 2.0 and 1.8 Å for cholic and chenodeoxycholic acids, respectively. As shown in Figure 2a, RamR binds two molecules of either cholic or chenodeoxycholic acid per dimer. Both compounds were completely enclosed by the RamR-binding pockets. The structural difference between cholic and chenodeoxycholic acid lies in the presence or absence of a 12-hydroxyl group (Fig. 1b), which in turn results in a difference in the electron density maps of RamR bound to these compounds (Fig. 2b, indicated by red arrows). Comparison of the ligated structures with unligated RamR revealed that the binding of cholic or chenodeoxycholic acid triggers uncoiling of the α7b and α8a helices (Fig. 2c), suggesting that RamR recognizes these compounds via an induced-fit mechanism. The binding position of cholic or chenodeoxycholic acid collides with helix α7b (indicated by a red ribbon in Fig. 2c) of the unliganded RamR. Thus, the uncoiling of α7b of RamR

(indicated as a green ribbon in Fig. 2c) is

required for the binding of these bile acid components. The α8a helix is also uncoiled in ligated RamR, probably because of the uncoiling of α7b. These uncoiled forms of α7b and α8a were not observed in RamR structures bound to multiple other drugs (Fig. 2d),[12] indicating that this helix uncoiling is required for the recognition of bile acids. Although the five antimicrobial drugs were found to form π–π interactions with Phe155 in a previous RamR structural study, this interaction does not occur with cholic or chenodeoxycholic acids (Fig. 3a). Instead of a π–π interaction, both bile acids form four hydrogen bonds with the Tyr59, Thr85, Ser137 and Asp152 residues of RamR (Fig. 3b). This indicates that both cholic and chenodeoxycholic acids are recognized by RamR via the same mechanism. These interactions are different from the hydrogen bonds formed by the five antimicrobial drugs with other amino acid residues of RamR, indicating that the mechanism of bile acid recognition is separate to those of other antimicrobial drugs. The interaction of different sets of amino acid residues with each compound indicates that multiple compounds are recognized by the multisite-binding pocket of RamR.

Reduction of RamR DNA-binding affinity by cholic acid and chenodeoxycholic acid

Baucheron *et al.* proposed that RamR interacts with P_{ramA} as a dimer of dimers.[14] We previously showed that the binding of multiple compounds to RamR reduces its DNA-binding affinity and results in the induction of *ramA* expression.[12] The results of the present study suggest that the binding of cholic acid or chenodeoxycholic acid to RamR may also reduce its DNA-binding affinity. To quantify the effects of cholic and chenodeoxycholic acids on the interaction of RamR with its DNA-binding site, we performed SPR experiments using a purified RamR protein and 100-bp DNA fragment containing the RamR-binding site. RamR protein solution was passed over the DNA fragment immobilized on a sensor chip while in the presence or absence of cholic or chenodeoxycholic acid (up to 500 μM). Both bile acids inhibited the binding of RamR to the DNA, in a concentration-dependent manner (Fig. 4). The IC_{50} values of cholic and chenodeoxycholic acids derived from the SPR data were 33.0 μM and 19.2 μM, respectively. In contrast, the much higher IC_{50} value obtained with deoxycholic acid (318 μM) indicated a much weaker ability of this bile acid to reduce the RamR

DNA-binding affinity (Fig. 4). This result is in good agreement with the qRT-PCR data, showing a lower activation of *ramA* expression by deoxycholic acid than by cholic and chenodeoxycholic acids (Fig. 1c).

Collectively, these results demonstrate that the interaction of cholic and chenodeoxycholic acids with RamR reduce its DNA-binding affinity and induce *ramA* expression.

Discussion

RamA is known to be a major activator protein of the AcrAB-TolC efflux system in *S.* Typhimurium, thus, it is involved in resistance to multiple drugs. Here, we report a regulatory mechanism for the expression of *ramA* that involves the binding of its local RamR repressor protein to bile acids. The DNA-binding activity of RamR appears to be controlled by major bile acids, such as cholic or chenodeoxycholic acids.

The transcription of *acrAB* and *tolC* in *Salmonella* was previously known to be activated by bile.[8] However, the regulatory mechanisms involved in this activation have not been reported. The activation of *acrAB* in *Salmonella* in response to bile seems to be independent of other regulatory proteins, such as MarRAB, Rob, RpoS or PhoP-PhoQ.[8] Since the AcrAB-TolC efflux system exports bile salts and functions in both the bile resistance [15] and pathogenesis of *Salmonella*,[7, 16, 17] it is important to understand the regulatory mechanism(s) of the *acrAB* and *tolC* genes in response to bile. We previously reported that bile induces AcrAB efflux pump expression in *Salmonella* through a specific regulatory protein, RamA, and, additionally, that cholic acid appears able to bind to this protein.[9] More recently, we also identified a different induction mechanism of *acrAB* in response to bile, whereby the bile-mediated activation of the *acrAB* and *tolC* multidrug efflux genes occurs via transcriptional derepression of the *ramA* activator gene, likely via the RamR repressor protein controlling expression of *ramA*.[10] Although the relative importance of both mechanisms has not yet been investigated, we suspect that these two different modes of regulation may coexist. A possible scenario is that bile first binds to and activates RamA and then, when the concentration of bile increases, proceeds to bind to RamR and stimulates RamA expression and the subsequent overproduction of the AcrAB-TolC efflux system. This scenario, however, requires further careful investigation.

The crystal structures of RamR in

complexes with the components of bile reveal that both cholic and chenodeoxycholic acids form four hydrogen bonds with the Tyr59, Thr85, Ser137 and Asp152 residues of RamR, instead of π–π interaction with Phe155, an important residue for the recognition of multiple other drugs. Both cholic and chenodeoxycholic acids, but not deoxycholic acid, induce *ramA* expression in a RamR-dependent manner. We tried to crystalize RamR bound to deoxycholic acid

but failed, probably because it lacks the 7α-hydroxyl group that is important in forming a hydrogen bond with Asp152 of RamR. Indeed, the inhibitory effect of deoxycholic acid on RamR-binding to the *ramA* promoter region is much weaker than that of cholic and chenodeoxycholic acids (Fig. 4). These acids inhibit interaction between RamR and the DNA fragment by approximately 90% or more at a concentration of 500 μM, whereas deoxycholic acid inhibits DNA binding by approximately 50% at the same concentration (Fig. 4b). This is consistent with the expression data, which show that deoxycholic acid induces *ramA* much less than cholic and chenodeoxycholic acids.

A similar approach to crystallizing a TetR-family regulator with bile acids has also been reported for CmeR,[18] and its structures complexed with taurocholic or cholic acids have been determined at resolutions of 2.2 and 2.4 Å, respectively. These two elongated bile acids did not bind in the same orientation inside the CmeR tunnel but, in fact, lay antiparallel to each other. The crystal structure of CmeR complexed with glycerol suggests the presence of at least two distinct binding sites[19], while the CmeR-bile acid structures indicated that the large taurocholic and cholic acid molecules did not span the predicted binding sites, but instead bound to a distinct second site and left the glycerol-binding site unoccupied.[18] Unlike

the bile acid-binding site in CmeR, the RamR-binding site of cholic and chenodeoxycholic acids is located on the upper side of the protein at almost the same position as that of the five antimicrobial drugs berberine, crystal violet, dequalinium, ethidium bromide and rhodamine 6G (Fig. 2d). The α7b and α8a helices were uncoiled in the structures of RamR in complex with

cholic and chenodeoxycholic acids, but such uncoiling was not observed in RamR bound to the five antimicrobial drugs or CmeR in complex with taurocholic or cholic acids. Uncoiling of the α7b and α8a helices probably occurred due to the smaller size of

the substrate-binding site of RamR compared to the relatively large cholic and chenodeoxycholic acid molecules.

Conclusion

In conclusion, we have extended our knowledge of the recognition of bile acids by RamR, a regulator of multidrug resistance in several enterobacterial pathogens.[20] Cholic and chenodeoxycholic acids both form four hydrogen bounds with RamR, instead of the π–π interaction that is important for recognition of other drugs. These different recognition mechanisms highlight the wide substrate specificity of RamR, whereby the substrate-binding pocket accommodates a diverse array of ligands.

Methods

Bacterial strains, plasmids and growth conditions

The *S. enterica* serovar Typhimurium strains were the wild-type strain ATCC14028s[21] and its Δ*ramR* mutant (which was produced as described previously).[22] Bacterial strains were grown at 37 °C in Luria–Bertani broth supplemented, when appropriate, with ampicillin (100 μg/ml), kanamycin (25 μg/ml) or chloramphenicol (25 μg/ml).

In order to investigate the effects of the bile acids on *ramA* expression, 25.6 mg/ml of a crude ox bile extract purchased under the label 'sodium choleate' (Sigma-Aldrich, S9875), or 5 mM sodium cholate hydrate, sodium chenodeoxycholate or sodium deoxycholate monohydrate (C6445, C8261 and D5670, respectively, and all from Sigma) was added to the medium. Sodium choleate, whose precise composition was not determined, has previously been used in *Salmonella* gene expression experiments at concentrations of 3% (w/v), i.e., 30 mg/mL or higher.[23] We chose a concentration of 25.6 mg/mL, because it was the highest concentration that allowed the normal growth of the *Salmonella* strains used in this study.

Gene expression analysis by qRT-PCR

Bacteria were grown until mid-log phase (OD_{600} of 0.6) and harvested by

centrifugation. Pelleted cells were stabilized with RNAprotect Bacteria Reagent (Qiagen) and stored at −80 °C until needed. Total RNA was extracted using an RNeasy Mini kit (Qiagen). Removal of residual genomic DNA was performed using a Turbo DNA-free kit (Ambion) and checked by negative PCR amplification of the chromosomal sequence. RNA integrity was verified by electrophoresis on a 1% agarose gel. Total RNA (1.5 μg) was reverse-transcribed using random hexamers and the Superscript III First Strand Synthesis System (Applied Biosystems). The expression level of each gene of interest was calculated as the average of the results from three independent cDNA samples. For each cDNA sample and each gene, qRT-PCR runs were performed in duplicated wells. The cycling conditions were: 95 °C for 5 min followed by 40 cycles of 95 °C for 10 s and then 60 °C for 15 s. After each run, amplification specificity and the absence of primer dimers were verified using a dissociation curve, acquired by heating the PCR products from 60 °C to 95 °C. The relative quantities of transcripts were determined using a standard curve and normalized against the geometric mean of three reference genes (*gmk*, *gyrB* and *rrs*). A two-tailed Student's *t* test was used to assess significance using a p value <0.05 as cutoff.

Crystallization, data collection, and structure determination

Purified RamR protein was prepared as described previously.[12] Co-crystals of RamR with cholic and chenodeoxycholic acids were grown from hanging drops at 25 °C using the vapor diffusion method. To form co-crystals, a 5-fold molar excess of cholic or chenodeoxycholic acids were added to 20 mg/ml RamR, then incubated overnight. The protein solution contained 20 mM sodium phosphate (pH 6.6), 75 mM NaCl and 2 mM DTT. The crystals grew to optimal size within 1 week and were cryoprotected using a solution containing 20% glycerol. Crystals were picked using LithoLoops (Protein Wave) and subjected to flash cooling in a cold nitrogen gas stream (100 K) from a cryostat (Oxford Cryosystems). All data sets were collected on beamline BL44XU at SPring-8 with a CCD detector MX225-HE (Rayonix) and at a cryogenic temperature of 100 K. The diffraction data were processed and scaled using the HKL2000[24] package. The crystal structures of bile-bound RamR were determined at 2.00 and 1.78 Å resolution by the molecular replacement method using the

program MOLREP[25] from the CCP4 software suite. The atomic coordinates of the ligand-free RamR (Protein Data Bank [PDB] code: 3VVX) were used as the search model. The model was refined with the CNS[26], REFMAC[27] and COOT[28] software and stereochemical quality was assessed with RAMPAGE software[29].

SPR analysis

The interaction between RamR and each substrate was analyzed by SPR spectroscopy with a Biacore T200 biosensor instrument (GE Healthcare). RamR was immobilized onto flow cells in a CM5 sensor chip using an amine-coupling method. Binding analyses were carried out at 25 ºC and a flow rate of 30 µl/min. Cholic and chenodeoxycholic acids were passed over the RamR at several concentrations, as indicated. An empty flow-cell lacking immobilized protein was used as a reference. The inhibitory effects of cholic, chenodeoxycholic and deoxycholic acids on the interaction between RamR and P_{ramA} were also analyzed by SPR spectroscopy. A 3′-biotinylated 100-bp DNA fragment of the *ramR–ramA* intergenic region, as well as a control 100-bp control fragment of the *gyrB* gene, were each immobilized onto flow cells in a NeutrAvidin (Thermo Scientific)-coated CM5 sensor chip (GE Healthcare). Analyses were performed at 25 °C and at a flow rate of 30 µl/min. The purified RamR protein was diluted in running buffer (10 mM HEPES, pH7.4, 150 mM NaCl, 1 mM EDTA, 0.05% v/v surfactant P20), incubated with 1.0–500 µM of cholic, chenodeoxycholic or deoxycholic acids, then injected onto the sensor surface in two replicates for 2 min. Dissociation was also recorded for 2 min. Calculations of affinity constants were performed using BIAevaluation software (GE Healthcare).

References

1. Prieto, A.I., Ramos-Morales, F. & Casadesus, J. Bile-induced DNA damage in *Salmonella enterica*. *Genetics* **168**, 1787-94 (2004).
2. Hernandez, S.B., Cota, I., Ducret, A., Aussel, L. & Casadesus, J. Adaptation and preadaptation of *Salmonella enterica* to Bile. *PLoS Genet* **8**, e1002459 (2012).
3. Prouty, A.M., Van Velkinburgh, J.C. & Gunn, J.S. *Salmonella enterica* serovar typhimurium resistance to bile: identification and characterization of the *tolQRA*

cluster. *J Bacteriol* **184**, 1270-6 (2002).

4. Begley, M., Sleator, R.D., Gahan, C.G. & Hill, C. Contribution of three bile-associated loci, *bsh*, *pva*, and *btlB*, to gastrointestinal persistence and bile tolerance of *Listeria monocytogenes*. *Infect Immun* **73**, 894-904 (2005).
5. Thanassi, D.G., Cheng, L.W. & Nikaido, H. Active efflux of bile salts by *Escherichia coli*. *J Bacteriol* **179**, 2512-8 (1997).
6. Gunn, J.S. Mechanisms of bacterial resistance and response to bile. *Microbes Infect* **2**, 907-13 (2000).
7. Nishino, K., Latifi, T. & Groisman, E.A. Virulence and drug resistance roles of multidrug efflux systems of *Salmonella enterica* serovar Typhimurium. *Mol Microbiol* **59**, 126-41 (2006).
8. Prouty, A.M., Brodsky, I.E., Falkow, S. & Gunn, J.S. Bile-salt-mediated induction of antimicrobial and bile resistance in *Salmonella typhimurium*. *Microbiology* **150**, 775-83 (2004).
9. Nikaido, E., Yamaguchi, A. & Nishino, K. AcrAB multidrug efflux pump regulation in *Salmonella enterica* serovar Typhimurium by RamA in response to environmental signals. *J Biol Chem* **283**, 24245-53 (2008).
10. Baucheron, S. *et al*. Bile-mediated activation of the *acrAB* and *tolC* multidrug efflux genes occurs mainly through transcriptional derepression of *ramA* in *Salmonella enterica* serovar Typhimurium. *J Antimicrob Chemother* **69**, 2400-6 (2014).
11. Abouzeed, Y.M., Baucheron, S. & Cloeckaert, A. *ramR* mutations involved in efflux-mediated multidrug resistance in *Salmonella enterica* serovar Typhimurium. *Antimicrob Agents Chemother* **52**, 2428-34 (2008).
12. Yamasaki, S. *et al*. The crystal structure of multidrug-resistance regulator RamR with multiple drugs. *Nat Commun* **4**, 2078 (2013).
13. Hofmann, A.F., Hagey, L.R. & Krasowski, M.D. Bile salts of vertebrates: structural variation and possible evolutionary significance. *J Lipid Res* **51**, 226-46 (2010).
14. Baucheron, S. *et al*. Binding of the RamR repressor to wild-type and mutated promoters of the RamA gene involved in efflux-mediated multidrug resistance in *Salmonella enterica* serovar Typhimurium. *Antimicrob Agents Chemother* **56**,

942-8 (2012).

15. Lacroix, F.J. *et al. Salmonella typhimurium acrB*-like gene: identification and role in resistance to biliary salts and detergents and in murine infection. *FEMS Microbiol Lett* **135**, 161-7 (1996).
16. Baucheron, S., Mouline, C., Praud, K., Chaslus-Dancla, E. & Cloeckaert, A. TolC but not AcrB is essential for multidrug-resistant *Salmonella enterica* serotype Typhimurium colonization of chicks. *J Antimicrob Chemother* **55**, 707-12 (2005).
17. Buckley, A.M. *et al.* The AcrAB-TolC efflux system of *Salmonella enterica* serovar Typhimurium plays a role in pathogenesis. *Cell Microbiol* **8**, 847-56 (2006).
18. Lei, H.T. *et al.* Crystal structures of CmeR-bile acid complexes from *Campylobacter jejuni*. *Protein Sci* **20**, 712-23 (2011).
19. Gu, R. *et al.* Crystal structure of the transcriptional regulator CmeR from *Campylobacter jejuni*. *J Mol Biol* **372**, 583-93 (2007).
20. Li, X.Z., Plesiat, P. & Nikaido, H. The challenge of efflux-mediated antibiotic resistance in Gram-negative bacteria. *Clin Microbiol Rev* **28**, 337-418 (2015).
21. Fields, P.I., Swanson, R.V., Haidaris, C.G. & Heffron, F. Mutants of *Salmonella typhimurium* that cannot survive within the macrophage are avirulent. *Proc Natl Acad Sci U S A* **83**, 5189-93 (1986).
22. Giraud, E., Baucheron, S., Virlogeux-Payant, I., Nishino, K. & Cloeckaert, A. Effects of natural mutations in the *ramRA* locus on invasiveness of epidemic fluoroquinolone-resistant *Salmonella enterica* serovar Typhimurium isolates. *J Infect Dis* **207**, 794-802 (2013).
23. Prouty, A.M., Brodsky, I.E., Falkow, S. & Gunn, J.S. Bile-salt-mediated induction of antimicrobial and bile resistance in *Salmonella typhimurium*. *Microbiology* **150**, 775–83 (2004).
24. Otwinowski, Z. & Minor, W. Processing of X-ray diffraction data collected in oscillation mode. *Methods Enzymol.* **276**, 307-326 (1997).
25. Vagin, A. & Teplyakov, A. MOLREP: an automated program for molecular replacement. *J. Appl. Cryst.* **30**, 1022-1025 (1997).
26. Brunger A.T., Adams P.D., Clore G.M., Gros P., Grosse-Kunstleve

R.W., Jiang J.-S., Kuszewski J., Nilges N., Pannu N.S., Read R.J., Rice L.M., Simonson T., Warren G.L.,Crystallography & NMR System (CNS), A new software suite for macromolecular structure determination, *Acta Cryst.* D **54**, 905-921(1998).

27. Murshudov, G. N., Vagin, A. A. & Dodson, E. J. Refinement of macromolecular structures by the maximum-likelihood method. *Acta Cryst.* D **53**, 240-255 (1997).

28. Emsley, P. & Cowtan, K. Coot: model-building tools for molecular graphics. *Acta Cryst.* D **60**, 2126-2132 (2004).

29. Lovell S.C., Davis I.W., Arendall W.B.3rd, de Bakker P.I., Word J.M., Prisant M.G., Richardson J.S. & Richardson D.C. Structure validation by Calpha geometry: phi,psi and Cbeta deviation. *Proteins: Structure, Function & Genetics.* **50**,437-450 (2002).

Acknowledgments

I would like to thank the collaborators Suguru Yamasaki, Ryosuke Nakashima, Keisuke Sakurai, Sylvie Baucheron, Etienne Giraud, Benoît Doublet, and Axel Cloeckaert. This work is supported in part by the Waksman Foundation of Japan Inc. This collaborative work was published in Scientific Reports (9: 177, 2019).

Figures

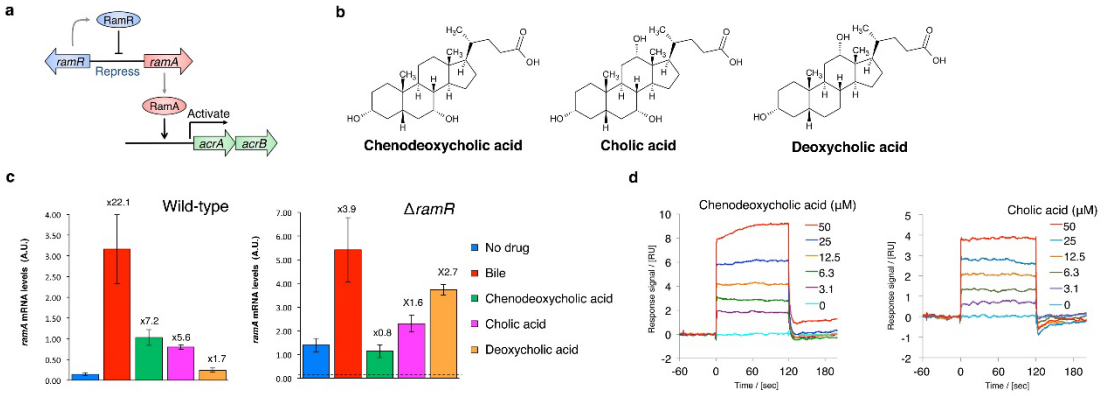

Figure 1. Chenodeoxycholic and cholic acids activate the *ramA* gene in a RamR-dependent manner. (**a**) Model for gene regulation pathway by RamR. RamR represses the *ramA* gene encoding the activator protein for the *acrAB* drug efflux pump genes. RamR binds to the region between the *ramR* and *ramA* genes, while RamA binds to the upstream region to *acrAB*. (**b**) The chemical structures of chenodeoxycholic acid, cholic and deoxycholic acids. (**c**) Effect of bile and chenodeoxycholic, cholic and deoxycholic acids on the expression of *ramA* in wild-type and Δ*ramR Salmonella* strains, as assessed by qRT-PCR. Cells were grown in LB broth supplemented with 25.6 mg/ml bile, or 5 mM of chenodeoxycholic, cholic or deoxycholic acids. Values above the bars indicate the fold difference in *ramA* mRNA levels relative to the control in the same strain (wild-type or Δ*ramR).* In the right panel (expression in Δ*ramR)*, the horizontal broken lines represents *ramA* mRNA levels in the wild-type control. The error bars indicate the standard deviation from three independent replicates. A.U., arbitrary units. (**d**) Binding of chenodeoxycholic and cholic acids to RamR detected by SPR analysis. RamR was immobilized onto a sensor chip and then the chenodeoxycholic or cholic acid was passed over the sensor surface at the various concentrations indicated. A representative result from one of three experiments that produced similar data is shown. SPR, surface plasmon resonance.

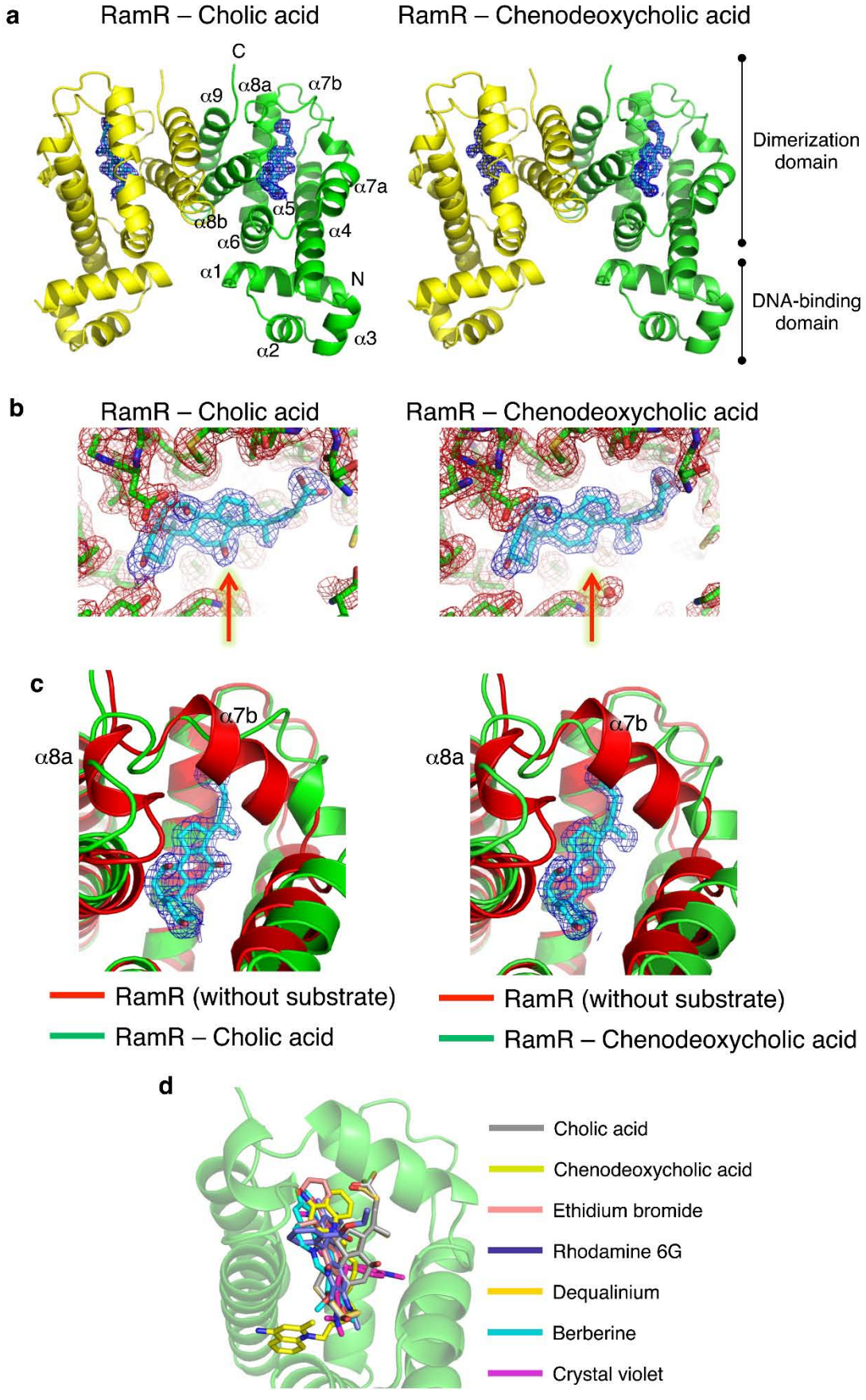
a
RamR – Cholic acid
RamR – Chenodeoxycholic acid
C
α9
α8a
α7b
α7a
α5
α8b
α4
α6
α1
N
α2
α3
Dimerization domain
DNA-binding domain
b
RamR – Cholic acid
RamR – Chenodeoxycholic acid
c
α8a
α7b
α8a
α7b
RamR (without substrate)
RamR – Cholic acid
RamR (without substrate)
RamR – Chenodeoxycholic acid
d
Cholic acid
Chenodeoxycholic acid
Ethidium bromide
Rhodamine 6G
Dequalinium
Berberine
Crystal violet

Figure 2. Co-crystal structures of RamR with cholic and chenodeoxycholic acids. (**a**) Full structure of the RamR dimer bound to two molecules of cholic or chenodeoxycholic acid. The α helices in RamR are indicated as α1, α2, α3, α4, α5, α6, α7a, α7b, α8a, α8b and α9. α7b and α8a are uncoiled upon the binding of cholic or chenodeoxycholic acid. $2F_o - F_c$ electron densities for cholic and chenodeoxycholic acids are show as a blue mesh contoured at 1.2σ. The carbon atoms of cholic or chenodeoxycholic acid are shown in cyan and oxygen atoms are shown in red. (**b**) Close-up view of the ligand binding site. Electron density map of the protein moiety (red mesh) and cholic and chenodeoxycholic acids (blue mesh) are contoured at 1.2σ. Carbon atoms of bile acid components and RamR are shown in cyan and green, respectively. Nitrogen, oxygen and sulfur atoms are shown in blue, red and yellow, respectively. The presence of a 12-hydroxyl group in cholic acid and its absence in chenodeoxycholic acid are indicated by red arrows. (**c**) Comparison of the unligated RamR structure (indicated as a red ribbon, PDB ID: 3VVX) with the ligated (cholic acid: 6IE8 or chenodeoxycholic acid: 6IE9) structures (indicated as green ribbons). $2F_o - F_c$ electron density for cholic acid and chenodeoxycholic acid is shown as a blue mesh, contoured at 1.2σ. Carbon atoms of cholic or chenodeoxycholic acids are shown in cyan, and oxygen atoms are shown in red. Superimposed structures indicate that binding of cholic acid or chenodeoxycholic acid triggers uncoiling of helices α7b and α8a. (**d**) The superposition of the RamR ligands determined in previous studies and this study. Carbon atoms of cholic acid (PDB ID: 6IE8), chenodeoxycholic acid (6IE9), ethidium bromide (3VVY), rhodamine 6G (3VVZ), dequalinium (3VW0), berberine (3VW2) and crystal violet (3VW1) are shown in gray, light green, pink, blue, yellow, light blue and purple, respectively. Other objects are colored as in Figure 2b. The imposed image indicates that the carboxyl groups of cholic and chenodeoxycholic acids are extended in the direction of the α7b helix. The binding locations of cholic and chenodeoxycholic acids are different from those observed for the five antimicrobial compounds.

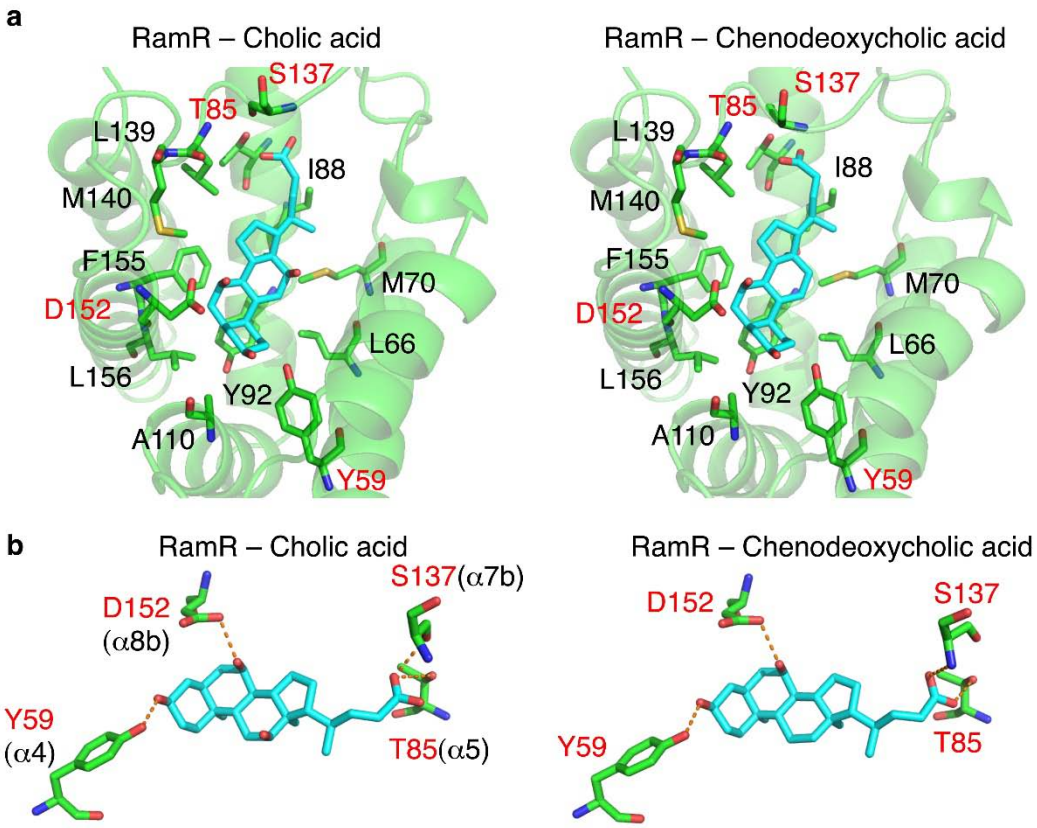

Figure 3. Recognition of bile acids by RamR. (**a**) The substrate-binding site of RamR with bound cholic and chenodeoxycholic acid molecules. Key residues that are involved in forming hydrogen bonds with cholic or chenodeoxycholic acid are shown, including Tyr59, Thr85, Ser137 and Asp152 (indicated by red characters). Objects are colored as in Figure 2. (**b**) Close-up view of the substrate-binding site of RamR containing cholic acid or chenodeoxycholic acid. Objects are colored as in Figure 2, and key residues are colored as in Figure 2a. Hydrogen bonds are indicated by dotted red lines.

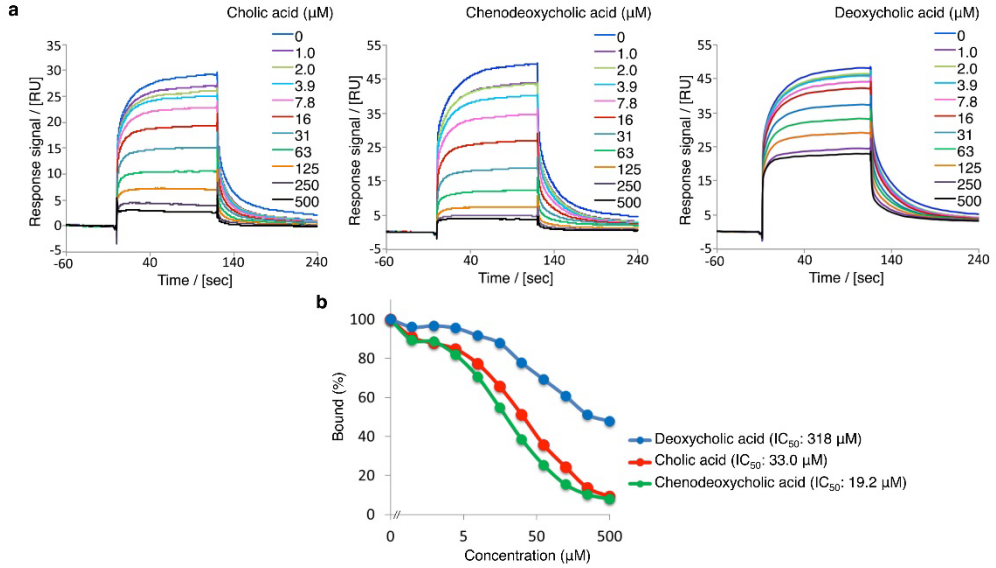

Figure 4. Inhibitory effects of bile acids on the DNA affinity of RamR. (**a**) Inhibitory effects of cholic or chenodeoxycholic acid on the DNA-binding affinity of RamR analyzed by SPR. DNA was immobilized onto a sensor chip and purified RamR protein was passed over the sensor surface in the presence or absence of bile acids at the various concentrations indicated. (**b**) Inhibitory effects were calculated from the results of SPR analysis. Percentage binding was calculated relative to the amount of RamR-binding to DNA in the absence of bile acids, which was assigned as 100%. The result of one of three experiments that produced similar data is shown. SPR, surface plasmon resonance.